Highlights

Oscillatory instabilities in dynamically active signalling compartments coupled via bulk diffusion in a 3-D spherical domain

Sarafa Iyaniwura, Michael J. Ward

- Derivation of an ODE system for a cell-bulk ODE-PDE model in a bounded 3-D domain in the near well-mixed limit. The effect of spatial inhomogeneities in the cell population is incorporated by the Neumann Green's matrix, and there is a diffusion parameter.

- Hopf bifurcations in the ODE system trigger intracellular oscillations as predicted by global bifurcation diagrams computed with MATCONT. Synchronization is studied via the Kuramoto order parameter.

- Quorum-sensing collective dynamics are illustrated as the number of cells exceeds a threshold, or as the spatial configuration of cells is varied. Through numerical experiments it is shown that a *single additional cell* can trigger intracellular oscillations in the entire cell population, which otherwise would not occur without this added cell.

- In the non well-mixed limit, where spatial effects are important, a novel integro-differential system is derived to characterize intracellular oscillations.

Oscillatory instabilities in dynamically active signalling compartments coupled via bulk diffusion in a 3-D spherical domain

Sarafa Iyaniwura[a], Michael J. Ward[b]

[a]Theoretical Biology and Biophysics, Theoretical Division, Los Alamos National Laboratory, Los Alamos, NM, 87545, USA
[b]Dept. of Mathematics, University of British Columbia, Vancouver, B.C., Canada, V6T 1Z2 (corresponding author)

Abstract

For a coupled cell-bulk ODE-PDE model in a 3-D spherical domain, we analyze oscillatory dynamics in spatially segregated dynamically active signalling compartments that are coupled through a passive extracellular bulk diffusion field. Within the confining spherical domain, the signalling compartments are a collection of small spheres of a common radius $\mathcal{O}(\varepsilon) \ll 1$. In our cell-bulk model, each cell secretes a signalling chemical into the extracellular bulk region, while also receiving a chemical feedback that is produced by all the other cells. This secretion and global feedback of chemical into the cells is regulated by permeability parameters on the cell membrane. In the near well-mixed limit corresponding to a large bulk diffusivity $D = D_0/\varepsilon \gg 1$, where $D_0 = \mathcal{O}(1)$, the method of matched asymptotic expansions is used to reduce the cell-bulk model to a novel nonlinear ODE system for the intracellular concentrations and the spatially averaged bulk diffusion field. The novelty in this ODE system, as compared to the type of ODE system that typically is studied in the well-mixed limit, is that it involves D_0 and an $\mathcal{O}(\varepsilon)$ correction term that incorporates the spatial configuration of the signalling compartments. For the case of Sel'kov intracellular kinetics, this new ODE system is used to study Hopf bifurcations that are triggered by the global coupling. In addition, the Kuramoto order parameter is used to study phase synchronization for the leading-order ODE system for a heterogeneous population of cells where some fraction of the cells have a random reaction-kinetic parameter. For a small collection of six cells, the spatial configuration of cells is also shown to influence both quorum-sensing behavior and diffusion-mediated communication that lead to synchronous intracellular oscillations. Moreover, we show that a single additional pacemaker cell can trigger intracellular oscillations in the other six cells, which otherwise would not occur. Finally, for the non well-mixed regime where $D = \mathcal{O}(1)$, we use asymptotic analysis in the limit $\varepsilon \to 0$ to derive a new integro-differential ODE system for the intracellular dynamics.

Keywords: Bulk diffusion, Green's function, synchronous oscillations, Kuramoto order parameter, Hopf bifurcation, quorum-sensing, strong localized perturbation theory, integro-differential systems.

---

1. Introduction

Bacteria and other microorganisms communicate and coordinate their activities in order to accomplish tasks that cannot be achieved by a single cell. Cells that are not in close proximity communicate via their extracellular environment through both the secretion of a signalling chemical into the extracellular medium and the absorption of the global concentration field that is produced by all the other cells. This feedback enables the cells to adjust their intracellular dynamics accordingly. Examples of biological systems that exhibit this kind of communication include a colony of starving yeast cells in which the exchange of acetaldehyde (Ace) molecules leads to glycolytic oscillations (cf. [1, 2, 3]), a collection of social amoebae *Dictyostelium discoideum*, where the secretion of cyclic adenosine monophosphate (cAMP) by the cells leads to synchronous oscillation in their intracellular dynamics and guides them to aggregation (cf. [4, 5, 6]), and a colony of the marine bacterium *Vibrio fischeri* that leads to bioluminescence in certain species of tropical squid (cf. [7, 8]).

This type of intracellular communication through a bulk diffusion field is closely associated with *quorum sensing (QS)*, a phenomenon by which the onset of collective intracellular dynamics occurs when the cell density increases past a threshold. Mathematical models of quorum-sensing usually focus on the well-mixed limit where the bulk diffusion field is spatially uniform. In other non well-mixed situations where spatial effects are important, the bulk diffusivity and bulk degradation control the onset of collective intracellular dynamics through spatial gradients, a phenomenon referred to as *diffusion sensing (DS)* or *diffusion-mediated synchronization*. QS systems are categorized into two main groups. The first group includes yeast cells and social amoeba, where a switch-like transition leads to synchronous oscillations as the cell population density passes a threshold (cf. [4, 9, 10, 3, 2, 1]). Physiochemical systems involving groups of catalyst-loaded small particles immersed in a Belousov-Zhabotinsky reaction mixture are also known to exhibit collective chemical oscillations (cf. [11, 12, 13, 14]). The second group of QS system includes a colony of the marine bacterium *Vibrio fischeri* and the human pathogen *Pseudomonas aeruginosa*, where a sudden transition between bistable steady-states occurs as the cell population density exceeds a certain threshold (cf. [15, 16, 8, 17]).

Various mathematical modeling frameworks have been developed to study the mechanism through which communication is achieved between spatially segregated active cells [18, 19, 20, 21, 22]. In this paper, we extend the coupled 2-D cell-bulk ODE-PDE model of [18, 23, 24] to a 3-D spherical domain, where the cells are small spheres of a common radius within the domain (see Fig. 1). Our model is inspired by the 3-D cell-bulk model formulated in [19, 20, 25] in all of $\mathbb{R}^3$, where there was a single intracellular species within each cell and where the bulk medium was purely diffusive. By allowing for multi-component intracellular species in a finite 3-D domain, and including both bulk diffusion and bulk degradation, we will show that our extended cell-bulk model can lead to synchronous intracellular oscillations. In our model, the secretion of a signalling molecule and the global feedback from the bulk medium are regulated by permeability parameters on the cell membrane, while spatio-temporal bulk diffusion fields in the extracellular medium are modeled explicitly with a PDE. This latter feature is in contrast to the approach in [22] where heterogeneity in the extracellular medium was modeled with a discrete diffusion equation, and in [21] where the signalling compartments were globally coupled through an ODE. Our main goal is to use the 3-D cell-bulk model to study the emergence and synchronization of intracellular oscillations that is mediated by the bulk diffusion field. We also investigate mechanisms that promote either quorum sensing or diffusion-mediated synchronization.

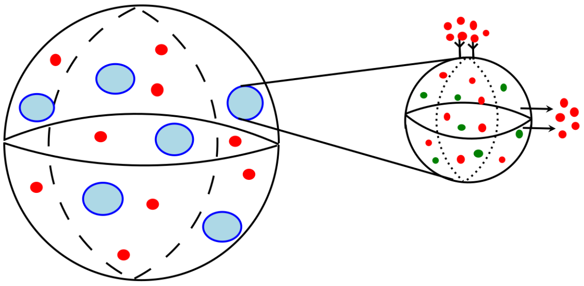

Figure 1: A schematic diagram showing dynamically active signalling compartments (in blue) in a 3-D spherical domain. Each signalling compartment is a smaller sphere containing two chemical species represented by the green and red dots, where only the red chemical is secreted into the extracellular bulk region. Right panel: Zoomed-in illustration of the intracellular concentration of chemicals within each signalling compartment, the secretion of signalling molecules into the bulk region, and the feedback of chemical into the cells.

The formulation of our coupled ODE-PDE model is as follows. Let $\Omega \subset \mathbb{R}^3$ be a bounded spherical domain of radius L containing m signalling compartments, denoted by Ω_j for $j = 1, \ldots, m$, which are smaller spheres of radius R, centered at $\mathbf{X}_j \in \Omega$ for $j = 1, \ldots, m$. In the bulk region $\Omega \setminus \cup_{j=1}^{m} \Omega_j$ and for $T > 0$, the concentration $\mathcal{U}(\mathbf{X}, T)$ of the bulk signalling species or autoinducer satisfies

$$\mathcal{U}_T = D_B \Delta \mathcal{U} - k_B \mathcal{U}\,, \quad \mathbf{X} \in \Omega \setminus \cup_{j=1}^{m} \Omega_j\,, \tag{1.1a}$$

$$\partial_{n_{\mathbf{X}}} \mathcal{U} = 0\,, \quad \mathbf{X} \in \partial\Omega\,, \tag{1.1b}$$

$$D_B \partial_{n_{\mathbf{X}}} \mathcal{U} = \beta_{1j} \mathcal{U} - \beta_{2j} \mu_j^1\,, \quad \mathbf{X} \in \partial\Omega_j\,, \quad j = 1, \ldots, m\,, \tag{1.1c}$$

where $D_B > 0$ and $k_B > 0$ are the dimensional diffusivity and decay rate of the bulk species, respectively, $\beta_{1j} > 0$ and $\beta_{2j} > 0$ are the dimensional rate of influx and efflux of chemical into and out of the j^{th} cell, respectively, and $\partial_{n_{\mathbf{X}}}$ denotes the outer normal derivative on Ω, which points into the bulk region. We assume that there are n interacting non-diffusing species within each cell represented by the vector $\mu_j \equiv (\mu_j^1, \ldots, \mu_j^n)^T$ for the j^{th} cell. Since the intracellular environment is assumed to be well-mixed, the n species are assumed to interact according to the local reaction-kinetics $\mathbf{F}_j(\mu/\mu_c)$. For each $j = 1, \ldots, m$, the intracellular dynamics within the j^{th} cell is coupled to the extracellular bulk diffusion field in (1.1) through the integration of the diffusive flux across the membrane of the cell as

$$\frac{d\mu_j}{dT} = k_R \mu_c \, \mathbf{F}_j \left(\mu_j / \mu_c \right) + \mathbf{e}_1 \int_{\partial\Omega_j} \left(\beta_{1j} \mathcal{U} - \beta_{2j} \mu_j^1 \right) \, \mathrm{d}S_{\mathbf{X}}\,. \tag{1.1d}$$

Here $\mathbf{e}_1 \equiv (1, 0, \ldots, 0)^T$, $k_R > 0$ is the reaction rate for the dimensionless local reaction kinetics $\mathbf{F}_j$, and $\mu_c > 0$

is a typical value for μ_j. Each cell secretes only one signalling chemical, labeled by μ_j^1, into the bulk medium as regulated by the efflux permeability parameter β_{2j}. The global feedback into the j^{th} cell, which is produced by the entire cell population, is regulated by the influx permeability parameter β_{1j}. A schematic illustration of the cell-bulk coupling in (1.1) is shown in Fig. 1 for $m = 6$ cells, each with $n = 2$ intracellular species.

For our asymptotic limit, we assume that the common radius R of the signalling compartments Ω_j for $j = 1, \ldots, m$ is small relative to the radius L of the spherical domain Ω. As such, we introduce a small scaling parameter $\varepsilon \equiv R/L \ll 1$. By non-dimensionalizing the coupled ODE-PDE model (1.1) as in Appendix A, we obtain that the dimensionless concentration $U(\mathbf{x}, t)$ in the bulk region satisfies for $t > 0$

$$\frac{\partial U}{\partial t} = D\Delta U - \kappa U\,, \quad \mathbf{x} \in \Omega \setminus \cup_{j=1}^{m} \Omega_{\varepsilon_j}\,, \tag{1.2a}$$

$$\partial_n U = 0\,, \quad \mathbf{x} \in \partial\Omega\,, \tag{1.2b}$$

$$\varepsilon D \partial_n U = d_{1j} U - \frac{d_{2j}}{\varepsilon} u_j^1\,, \quad \mathbf{x} \in \partial\Omega_{\varepsilon_j}\,, \quad j = 1, \ldots, m\,, \tag{1.2c}$$

which is coupled to the dimensionless intracellular dynamics within the j^{th} cell, for each $j = 1, \ldots, m$, by

$$\frac{\mathrm{d}\mathbf{u}_j}{\mathrm{d}t} = \mathbf{F}_j\left(\mathbf{u}_j\right) + \frac{\mathbf{e}_1}{\varepsilon^2} \int_{\partial\Omega_{\varepsilon_j}} \left(\varepsilon\, d_{1j}\, U - d_{2j}\, u_j^1\right) \mathrm{d}S_{\mathbf{x}}\,. \tag{1.2d}$$

Here $\mathbf{u}_j \equiv (u_j^1, \ldots, u_j^n)^T$ is a vector representing the dimensionless molar concentration of the n species in the j^{th} cell, labeled by $\Omega_{\varepsilon j} \equiv \{\mathbf{x} \,|\, |\mathbf{x} - \mathbf{x}_j| \le \varepsilon\}$. We assume that the cells are *well-separated* in the sense that $\operatorname{dist}(\mathbf{x}_j, \mathbf{x}_k) = O(1)$ for $j \neq k$ and $\operatorname{dist}(\mathbf{x}_j, \partial\Omega) = O(1)$ as $\varepsilon \to 0$. The key $O(1)$ parameters in the dimensionless cell-bulk model (1.2) are

$$D \equiv \frac{D_B}{k_R L^2}\,, \qquad \kappa \equiv \frac{k_B}{k_R}\,, \qquad d_{1j} \equiv \varepsilon \frac{\beta_{1j}}{k_R L}\,, \qquad d_{2j} \equiv \varepsilon^2 \frac{\beta_{2j} L^2}{k_R}\,. \tag{1.3}$$

Here D and κ are the effective diffusion coefficient and bulk decay rate of the bulk species, respectively. The scaling limit chosen for the permeability parameters is necessary to compensate for the small size of the cells relative to the volume of the domain, and the rapid decay of the 3-D free-space Green's function (see Appendix A). Since the bulk decay rate κ is the ratio of the dimensional bulk decay rate to the reaction rate of the intracellular kinetics, an increase in κ corresponds to an increase in the rate of degradation of the bulk species relative to the rate they are produced within the cells. In particular for large κ, the chemical signal secreted by the cells decays on a short length-scale, resulting in a rather weak coupling between the cells. In terms of the effective bulk diffusivity D, when D is large relative to κ, the spatial gradients in the bulk medium are weak and there is effectively a global coupling between the cells.

The outline of the paper is as follows. In the *near well-mixed limit* corresponding to a large bulk diffusivity $D = D_0/\varepsilon \gg 1$, with $D_0 = O(1)$, in §2 the method of matched asymptotic expansions is used to derive a novel ODE system from the cell-bulk ODE-PDE model (1.2). The novelty in this ODE system is that it involves D_0 and includes an $O(\varepsilon)$ correction term involving the Neumann Green's matrix that accounts for the spatial configuration of the small dynamically reactive cells. In this "near well-mixed limit", the resulting ODE system is similar in form to that for the 2-D case derived in §3 of [23], but without the additional scaling in the efflux permeability d_{2j} as in (1.2c).

For the special case of Sel'kov intracellular reaction kinetics, in §3 the leading-order dynamics for this ODE system, which sets $\epsilon = 0$ and thereby neglects the spatial configuration of cells, is analyzed to predict Hopf bifurcations that initiate intracellular oscillations for a collection of identical cells. In particular, we show that as the cell density parameter is increased it first triggers and then quenches intracellular oscillations in the population of cells. Moreover, for this leading-order system, quorum-sensing and phase synchronization of large amplitude intracellular oscillations, as monitored by a Kuramoto order parameter, are also studied numerically for a heterogeneous population of 1000 cells. In this total population, some fraction of the cells are taken to have a random reaction-kinetic parameter that modifies the local frequency of oscillation within each cell. As the fraction of such "defective cells" in the population increases, it is shown numerically that the range of the cell density parameter where in-phase synchronous oscillations occur decreases. In this sense, for our leading-order system, we conclude that "cell heterogeneity" does not promote the in-phase syncronization of intracellular oscillations. Our findings conform to the widely held assumption for coupled non-identical oscillators that disorder is undesirable for synchronization (cf. [26], [27]). However, we remark that it has recently been established that a time-delay in the coupling function actually enhances synchronization for non-identical coupled Stuart-Landau oscillators (cf. [28]).

In §4, we study the $O(\epsilon)$ effect of the spatial configuration of cells on intracellular dynamics by considering three distinct configurations of six cells in the unit sphere. For this small cell population, where we assume that the reaction-kinetic parameters and membrane permeabilites are identical for each cell, "cell heterogeneity" only arises from choosing different spatial configurations of the cells. We consider three cell configurations: cells whose centers are symmetrically located on a concentric spherical ring within the sphere, cells whose centers are arbitrarily located on the concentric ring within the sphere, and cells that are arbitrarily located within the sphere. For the first two patterns, where the cells are centered on a concentric ring within the sphere, the effect of the nearest image or "ghost" cell across the reflecting domain boundary is the same for each cell. For these two ring configurations of cells, it is shown numerically that the range of the bulk degradation κ where intracellular oscillations occur is larger for the disordered arrangement than when cells are equally-spaced on the concentric ring. With disorder, since at least two cells will be in closer proximity than for the equally-spaced arrangement, the communication between these two cells through the bulk medium will be relatively strong even when the bulk decay rate κ increases. These two cells can then trigger intracellular oscillations for the entire cell population. In this sense, this type of cell heterogeneity promotes intracellular oscillations. Moreover, for a fixed κ, the Kuramoto order parameter is computed to show that diffusion-mediated synchronization can be achieved as D_0 is increased, even when the cells are arbitrarily located within the sphere with no two cells in close proximity. For each of the three spatial configurations of cells considered in §4, in §5 we illustrate QS behavior by showing that a *single pacemaker* cell can trigger synchronous intracellular dynamics in the entire population of six cells, which otherwise would be in a quiescent state without this additional cell.

In §6 we derive a new integro-differential ODE system for intracellular dynamics for the non-well mixed case where $D = O(1)$. This new result shows that the interaction between the cells and the bulk is only $O(\varepsilon) \ll 1$ in this $D = O(1)$ regime. This is in direct contrast to the 2-D case analyzed in [29] in all of $\mathbb{R}^2$ where the interaction is much stronger at $O(-1/\log\varepsilon)$. However, when $D \gg 1$, and under a re-scaling of the efflux permeability, we show in §6.1 that this integro-differential system reduces to leading order to our ODE system derived in §2, where cell-bulk interactions are $O(1)$.

Finally, in §7 we briefly summarize our results and discuss some open directions, including extending our approach to allow for biologically realistic models of quorum-sensing in bacteria.

2. Asymptotics of the cell-bulk model for large *D*

In the limit $\varepsilon \to 0$, we use strong localized perturbation theory [30] to analyze (1.2) in the regime of a fast diffusing bulk species and a large rate of global feedback into the cells. Our goal is to derive an ODE system that has a diffusion parameter and also a weak perturbation term that incorporates the spatial configuration of cells.

We begin our analysis by rescaling the effective bulk diffusivity D and the influx permeability d_{1j} as

$$D = \frac{D_0}{\varepsilon} \quad \text{and} \quad d_{1j} = \frac{\widetilde{d}_{1j}}{\varepsilon}, \quad j = 1, \ldots, m, \tag{2.1}$$

where $D_0 \equiv O(1)$ and $\widetilde{d}_{1j} \equiv O(1)$. With this scaling, dimensionless bulk concentration for $t > 0$ satisfies

$$\frac{\partial U}{\partial t} = \frac{D_0}{\varepsilon}\Delta U - \kappa U\,, \quad \mathbf{x} \in \Omega \setminus \cup_{j=1}^{m} \Omega_{\varepsilon_j}\,, \tag{2.2a}$$

$$\partial_n U = 0\,, \quad \mathbf{x} \in \partial\Omega\,, \tag{2.2b}$$

$$\varepsilon D_0 \partial_n U = \widetilde{d}_{1j} U - d_{2j} u_j^1\,, \quad \mathbf{x} \in \partial\Omega_{\varepsilon_j}\,, \quad j = 1, \ldots, m\,, \tag{2.2c}$$

which is coupled to the dynamics within the j^{th} cell by

$$\frac{d\mathbf{u}_j}{dt} = \mathbf{F}_j\left(\mathbf{u}_j\right) + \frac{\mathbf{e}_1}{\varepsilon^2}\int_{\partial\Omega_{\varepsilon_j}} \left(\widetilde{d}_{1j} U - d_{2j} u_j^1\right)\, \mathrm{d}S_{\mathbf{x}}\,, \tag{2.2d}$$

for $j = 1, \ldots, m$.

For $D = D_0/\varepsilon \gg O(1)$, we expand $U(\mathbf{x}, t)$ in the outer region at $O(1)$ distances from the cells as

$$U(\mathbf{x}, t) = U_0(\mathbf{x}, t) + \frac{\varepsilon}{D_0} U_1(\mathbf{x}, t) + \ldots\,. \tag{2.3}$$

Upon substituting (2.3) into (2.2) and collecting terms in powers of ε, we obtain the leading-order problem

$$\Delta U_0 = 0\,, \quad \mathbf{x} \in \Omega\,; \quad \partial_n U_0 = 0\,, \quad \mathbf{x} \in \partial\Omega\,, \tag{2.4}$$

for which $U_0 \equiv U_0(t)$ is the solution. The next-order problem for U_1 in the outer region is

$$\begin{aligned} &\Delta U_1 = U_0' + \kappa U_0\,, \quad \mathbf{x} \in \Omega \setminus \{\mathbf{x}_1, \ldots, \mathbf{x}_m\}\,, \\ &\partial_n U_1 = 0\,, \quad \mathbf{x} \in \partial\Omega\,, \end{aligned} \tag{2.5}$$

where we must determine the appropriate singularity behavior of U_1 as $\mathbf{x} \to \mathbf{x}_j$ for each $j = 1, \ldots, m$.

In the inner region, defined at an $\mathcal{O}(\varepsilon)$ neighborhood of the j^{th} cell, we introduce the inner variables $\mathbf{y} = \varepsilon^{-1}(\mathbf{x} - \mathbf{x}_j)$ and $U(\mathbf{x}, t) = V_j(\mathbf{x}_j + \varepsilon\mathbf{y}, t)$, with $r = |\mathbf{y}|$. Upon writing (2.2a) and (2.2c) in terms of the inner variables, we obtain for each $j = 1, \ldots, m$ that as $\varepsilon \to 0$,

$$\begin{aligned} &\Delta_r V_j = 0\,, \quad r > 1\,; \quad V_j \to v_{j\infty} \quad \text{as} \quad r \to \infty\,, \\ &D_0\,\partial_r V_j = \widetilde{d}_{1j} V_j - d_{2j} u_j^1\,, \quad \text{on} \quad r = 1\,, \end{aligned} \tag{2.6}$$

where $\Delta_r \equiv \partial_{rr} + 2r^{-1}\partial_r$, and $v_{j\infty}$ is the constant far-field behaviour, which may depend on ε. The solution to (2.6) is

$$V_j = \frac{c_j}{r} + v_{j\infty} \quad \text{where} \quad c_j = \frac{d_{2j}u_j^1 - \widetilde{d}_{1j} v_{j\infty}}{\widetilde{d}_{1j} + D_0}\,. \tag{2.7}$$

Upon matching the inner solution (2.7) to the outer expansion in (2.3), we obtain a singularity behavior for U_1 as $\mathbf{x} \to \mathbf{x}_j$. In terms of a delta distribution, the singularity behavior for U_1 is combined with (2.5) to derive the complete outer problem for U_1 given by

$$\begin{aligned} &\Delta U_1 = U_0' + \kappa U_0 - 4\pi D_0 \sum_{i=1}^{m} c_i \delta(\mathbf{x} - \mathbf{x}_i)\,, \quad \mathbf{x} \in \Omega\,, \\ &\partial_n U_1 = 0\,, \quad \mathbf{x} \in \partial\Omega\,; \quad \int_\Omega U_1\, d\mathbf{x} = 0\,, \end{aligned} \tag{2.8}$$

where c_i is as defined in (2.7) and $\delta(\mathbf{x} - \mathbf{x}_i)$ is the Dirac delta function localized at the center of the i^{th} cell. Without loss of generality, we impose $\int_\Omega U_1\, \text{d}\mathbf{x} = 0$, so that the spatial average of U in the bulk region is U_0, i.e. $U_0 = (1/|\Omega|) \int_\Omega U\, \text{d}\mathbf{x}$. By using the divergence theorem, the solvability condition for (2.8) yields the ODE

$$U_0' + \kappa U_0 = \frac{4\pi D_0}{|\Omega|} \sum_{i=1}^{m} c_i\,, \tag{2.9}$$

where $|\Omega|$ is the domain volume. When this solvability condition holds, we write the solution to (2.8) in terms of the Neumann Green's function $G(\mathbf{x}; \mathbf{x}_j)$ satisfying

$$\Delta G = \frac{1}{|\Omega|} - \delta(\mathbf{x} - \mathbf{x}_j) \quad \mathbf{x} \in \Omega\,, \tag{2.10a}$$

$$G(\mathbf{x}; \mathbf{x}_j) \sim \frac{1}{4\pi|\mathbf{x} - \mathbf{x}_j|} + R_j\,, \quad \text{as} \quad \mathbf{x} \to \mathbf{x}_j\,, \tag{2.10b}$$

$$\partial_n G = 0\,, \ \ \mathbf{x} \in \partial\Omega\,; \qquad \int_\Omega G\, \text{d}\mathbf{x} = 0\,, \tag{2.10c}$$

where $R_j \equiv R(\mathbf{x}_j)$ is its regular part at $\mathbf{x} = \mathbf{x}_j$. The solution to the outer problem (2.8) is simply

$$U_1 = 4\pi D_0 \sum_{i=1}^{m} c_i G(\mathbf{x}; \mathbf{x}_i)\,. \tag{2.11}$$

Expanding (2.11) as $\mathbf{x} \to \mathbf{x}_j$ and using the singularity behaviour of the Neumann Green's function given in (2.10b), we obtain for each $j = 1, \ldots, m$ that

$$U_1 \sim \frac{D_0\, c_j}{|\mathbf{x} - \mathbf{x}_i|} + 4\pi D_0 \left(\mathcal{G}\mathbf{c}\right)_j + o(1)\,, \quad \text{as} \quad \mathbf{x} \to \mathbf{x}_j\,, \tag{2.12}$$

where $\mathbf{c} = (c_1, \ldots, c_m)^T$ and $\mathcal{G}$ is the symmetric Neumann Green's matrix whose entries are defined by

$$(\mathcal{G})_{ij} = (\mathcal{G})_{ji} = G(\mathbf{x}_i, \mathbf{x}_j), \ \ i \neq j\,; \quad (\mathcal{G})_{jj} = R_j \equiv R(\mathbf{x}_j)\,. \tag{2.13}$$

Upon substituting (2.12) into the outer expansion in (2.3) and matching the resulting expansion to the far-field behavior of the inner solution (2.7), we obtain as $\mathbf{x} \to \mathbf{x}_j$ that

$$v_{j\infty} + \frac{\varepsilon c_j}{|\mathbf{x} - \mathbf{x}_i|} \sim U_0 + \frac{\varepsilon c_j}{|\mathbf{x} - \mathbf{x}_i|} + 4\pi\varepsilon(\mathcal{G}\mathbf{c})_j + o(1)\,. \tag{2.14}$$

From (2.14), we derive the matching condition

$$v_{j\infty} = U_0 + 4\pi\varepsilon(\mathcal{G}\mathbf{c})_j \quad \text{where} \quad c_j = \frac{d_{2j}\, u_j^1 - \widetilde{d}_{1j}\, v_{j\infty}}{\widetilde{d}_{1j} + D_0}\,, \tag{2.15}$$

for each $j = 1, \ldots, m$. Observe that the two equations in (2.15) are coupled, since c_j also depends on $v_{j\infty}$. We solve these equations recursively for $\varepsilon \to 0$ to obtain

$$v_{j\infty} = U_0 + 4\pi\varepsilon(\mathcal{G}\tilde{\mathbf{c}})_j + \mathcal{O}(\varepsilon^2)\,, \tag{2.16a}$$

$$c_j = \tilde{c}_j - \frac{4\pi\varepsilon(\mathcal{G}\tilde{\mathbf{c}})_j \widetilde{d}_{1j}}{\widetilde{d}_{1j} + D_0} + \mathcal{O}(\varepsilon^2)\,, \tag{2.16b}$$

where

$$\tilde{c}_j \equiv \frac{d_{2j}u_j^1 - \widetilde{d}_{1j} U_0}{\widetilde{d}_{1j} + D_0}\,, \qquad j = 1, \ldots, m\,. \tag{2.16c}$$

Next, we return to the intracellular dynamics of the cells given in (2.2d). Upon evaluating the integral in (2.2d) over the boundary of the j^{th} cell, we obtain

$$\frac{d\mathbf{u}_j}{dt} = \mathbf{F}_j\left(\mathbf{u}_j\right) - 4\pi D_0 \mathbf{e}_1 c_j\,, \qquad j = 1, \ldots, m\,. \tag{2.17}$$

In deriving (2.17), we used $\partial_n U|_{\partial\Omega_{\varepsilon j}} = -D_0 \partial_r V_j|_{r=1} = -c_j$ on the boundary of the j^{th} cell. Upon substituting c_j as given in (2.16) into (2.9) and (2.17), we obtain an ODE for the spatially averaged bulk species U_0, which is coupled to an ODE system for the intracellular dynamics. In this way, we obtain the $nm + 1$ dimensional coupled ODE system

$$\begin{aligned} U_0' &= -\kappa\, U_0 + \frac{1}{|\Omega|} \sum_{j=1}^{m} \left(k_{2j} u_j^1 - k_{1j} U_0\right) \\ &\quad - \frac{4\pi\varepsilon}{|\Omega|} \sum_{j=1}^{m} k_{1j} (\mathcal{G}\tilde{\mathbf{c}})_j \,, \end{aligned} \tag{2.18a}$$

$$\begin{aligned} \frac{d\mathbf{u}_j}{dt} &= \mathbf{F}_j\left(\mathbf{u}_j\right) - \mathbf{e}_1\left(k_{2j} u_j^1 - k_{1j} U_0\right) \\ &\quad + 4\pi \mathbf{e}_1 \varepsilon k_{1j} (\mathcal{G}\tilde{\mathbf{c}})_j \,, \quad j = 1, \ldots, m \,, \end{aligned} \tag{2.18b}$$

where

$$\begin{aligned} k_{1j} &\equiv \frac{4\pi D_0 \widetilde{d}_{1j}}{\widetilde{d}_{1j} + D_0} \,, \quad k_{2j} \equiv \frac{4\pi D_0 d_{2j}}{\widetilde{d}_{1j} + D_0} \,, \\ \tilde{c}_j &\equiv \frac{d_{2j} u_j^1 - \widetilde{d}_{1j} U_0}{\widetilde{d}_{1j} + D_0} \,, \quad \tilde{\mathbf{c}} \equiv (\tilde{c}_1, \ldots, \tilde{c}_m)^T \,. \end{aligned} \tag{2.18c}$$

Here $\mathcal{G}$ is the Neumann Green's matrix, which depends on the shape of the domain Ω and the cell locations $\mathbf{x}_1, \ldots, \mathbf{x}_m$. Since the novel ODE system (2.18) contains D_0 and a correction term that incorporates the spatial configuration of the cells through the $\mathcal{G}$ matrix, it can be used to study both quorum and diffusion sensing. Moreover, since the coefficients of the correction terms in (2.18a) and (2.18b) are rather significant for moderately small values of ε, we expect that the spatial configuration $\mathbf{x}_1, \ldots, \mathbf{x}_m$ of the cells can influence whether or not intracellular oscillations are triggered.

3. Analysis of the leading-order dynamics

In this section, we first perform a Hopf bifurcation analysis on the leading-order dynamics of the ODE system (2.18) (when $\varepsilon = 0$) for identical cells in order to investigate the onset of intracellular oscillations that is triggered by the global coupling. This analysis is done for the two-component kinetics used in [31] to model chemical oscillations, which is a modification of the Sel'kov kinetics [32] used to model glycolysis oscillations. In addition, for this choice of kinetics, quorum sensing and phase synchronization in the intracellular dynamics for the leading-order dynamics is studied using the Kuramoto order parameter (cf. [22, 21, 24]).

3.1. Hopf bifurcation analysis for identical cells

We consider (2.18) in a spherical domain when $\varepsilon = 0$. In terms of a cell density parameter defined by $\rho \equiv m/|\Omega|$, which measures the number of cells per unit volume, the leading-order ODE system in (2.18) becomes

$$\begin{aligned} U_0' &= -\kappa\, U_0 - \frac{\rho}{m} \sum_{j=1}^{m} (k_{1j} U_0 - k_{2j} u_j^1) \,, \\ \frac{d\mathbf{u}_j}{dt} &= \mathbf{F}_j\left(\mathbf{u}_j\right) + \mathbf{e}_1 (k_{1j} U - k_{2j} u_j^1) \,, \quad j = 1, \ldots, m \,, \end{aligned} \tag{3.1a}$$

where k_{1j} and k_{2j} are defined in (2.18c).

For identical cells, where the permeabilities and the reaction-kinetics are the same we have $k_{1j} = k_1$, $k_{2j} = k_2$, and $\mathbf{F}(\mathbf{u}) \equiv \mathbf{F}_j(\mathbf{u}_j)$, with $\mathbf{u} \equiv \mathbf{u}_j$, for $j = 1, \ldots, m$. For this identical cell case, (3.1) reduces to

$$\begin{aligned} U_0' &= -\kappa U_0 - \rho (k_1 U_0 - k_2 u^1) \,, \\ \frac{d\mathbf{u}}{dt} &= \mathbf{F}\left(\mathbf{u}\right) + \mathbf{e}_1 (k_1 U - k_2 u^1) \,. \end{aligned} \tag{3.2}$$

For the reaction kinetics in [31], which we refer to as Sel'kov kinetics, we have $\mathbf{F} \equiv (f(v,w), g(v,w))^T$, with $\mathbf{u} = (u^1, u^2)^T \equiv (v, w)^T$, where

$$f = \alpha w + w v^2 - v \,, \quad g = \epsilon_0 \left[\mu - (\alpha w + w v^2)\right] \,. \tag{3.3}$$

The reaction-kinetic parameters α, μ, and ϵ_0 are all positive. Upon substituting (3.3) into (3.2), the steady-state solution for (3.2) is

$$\begin{aligned} u_e^1 &= \frac{\mu(\kappa + k_1 \rho)}{(\kappa + \kappa k_2 + \rho k_1)} \,, \quad u_e^2 = \frac{\mu}{(\alpha + (u_e^1)^2)} \,, \\ U_{0e} &= \frac{\mu \rho k_2}{(\kappa + \kappa k_2 + \rho k_1)} \,, \end{aligned} \tag{3.4}$$

where U_{0e} is the steady-state average concentration in the bulk region and $\mathbf{u}_e \equiv (u_e^1, u_e^2)^T$ is the steady-state intracellular concentration.

We perturb the steady-state solution (U_{0e}, u_e^1, u_e^2) as

$$U = U_{0e} + e^{\lambda t} \eta \,, \quad \mathbf{u} = \mathbf{u}_e + e^{\lambda t} \phi \,, \tag{3.5}$$

where $\eta \ll 1$ and $\phi \equiv (\phi_1, \phi_2)^T \ll 1$. Upon substituting (3.5) into (3.2), we obtain the linearized system

$$\lambda \eta = -\kappa \eta - \rho (k_1 \eta - k_2 \phi_1) \,, \quad \lambda \phi = J_e \phi + \mathbf{e}_1 (k_1 \eta - k_2 \phi_1) \,, \tag{3.6}$$

where J_e is the Jacobian matrix of the reaction kinetics $\mathbf{F}(\mathbf{u}) \equiv (f(u^1, u^2), g(u^1, u^2))^T$ evaluated at the steady-state $\mathbf{u}_e = (u_e^1, u_e^2)^T$. Labeling $(u_e^1, u_e^2) \equiv (v_e, w_e)$ and $\mathbf{F} = (f(v,w), g(v,w))^T$, we write (3.6) in matrix form as

$$\mathcal{H}(\lambda) \mathbf{\Psi} = \mathbf{0} \,. \tag{3.7}$$

where $\mathbf{\Psi} \equiv (\eta, \phi_1, \phi_2)^T$ and $\mathcal{H}(\lambda)$ is the 3×3 matrix

$$\mathcal{H}(\lambda) \equiv \begin{pmatrix} -(\kappa + \rho k_1) - \lambda & \rho k_2 & 0 \\ k_1 & (f_v^e - k_2 - \lambda) & f_w^e \\ 0 & g_v^e & (g_w^e - \lambda) \end{pmatrix}. \tag{3.8}$$

Here, f_v^e, f_w^e, g_v^e and g_w^e are the partials of f and g evaluated at $\mathbf{u}_e$. The characteristic polynomial for (3.7) is

$$\lambda^3 + q_1\lambda^2 + q_2\lambda + q_3 = 0\,, \tag{3.9}$$

with coefficients given by

$$\begin{aligned} q_1 &\equiv (\kappa + k_2 + \rho k_1) - \operatorname{tr}(J_e)\,, \\ q_2 &\equiv \det(J_e) - (\kappa + \rho k_1)\operatorname{tr}(J_e) + k_2\left(\kappa - g_w^e\right)\,, \\ q_3 &\equiv (\kappa + \rho k_1)\det(J_e) - \kappa k_2 g_w^e\,, \end{aligned} \tag{3.10}$$

where $\det(J_e) = f_v^e g_w^e - f_w^e g_v^e$ and $\operatorname{tr}(J_e) = f_v^e + g_w^e$ are the determinant and trace of the Jacobian J_e. For Sel'kov kinetics we readily calculate that $\det(J_e) = \epsilon_0(\alpha + v_e^2) > 0$ and $\operatorname{tr}(J_e) = 2w_e v_e - 1 - \epsilon_0(\alpha + v_e^2)$. By the Routh-Hurwitz criterion for cubic polynomials, we have $\operatorname{Re}(\lambda) < 0$ if and only if the following three conditions hold:

$$q_1 > 0\,, \quad q_3 > 0\,, \quad \text{and} \quad q_1 q_2 > q_3\,. \tag{3.11}$$

To determine Hopf bifurcation (HB) points, for which $\lambda_1 = a < 0$, $\lambda_{2,3} = \pm i\omega$, we must have $(\lambda - a)(\lambda - i\omega)(\lambda + i\omega) = \lambda^3 - a\lambda^2 + \omega^2\lambda - a\omega^2 = 0$ so that the coefficients in (3.9) must satisfy

$$q_1 > 0\,, \quad q_3 > 0\,, \quad \text{and} \quad q_1 q_2 = q_3\,, \tag{3.12}$$

at the HB points. This criterion is used below to compute HB points with respect to bifurcation parameters.

In the results below, the Sel'kov parameters in (3.3) and the influx and efflux permeabiliites are fixed at

$$\alpha = 0.9\,, \quad \epsilon_0 = 0.15\,, \quad \mu = 2\,, \quad \tilde{d}_1 = 0.8\,, \quad d_2 = 0.2\,. \tag{3.13}$$

The kinetics parameters α, ϵ_0 and μ have been selected so that the local dynamics of each cell is linearly stable when it is isolated from the bulk (i.e. $\operatorname{tr}(J_e) < 0$). Our goal is to seek an oscillatory instability in the intracellular dynamics that is triggered by the global coupling.

Next, we compute HB points of the leading-order ODE system (3.2) using the criteria in (3.12), parameters in (3.13), and with $D_0 = 0.5$ for $m = 6$ identical cells. Fixing $\kappa = 3.2$, the HB points with respect to the cell density are $\rho_1 = 0.3548$ and $\rho_2 = 5.2035$. Since $\rho = m/|\Omega|$ and $m = 6$ is fixed, varying ρ corresponds to varying the volume $|\Omega|$ of the domain Ω. Similarly, for a fixed cell density $\rho = 1.4324$ (corresponding to $m = 6$ cells in the unit sphere), the HB points with respect to the bulk decay parameter κ are $\kappa_1 = 1.5508$ and $\kappa_2 = 16.7815$. These HB points agree with the global bifurcation results shown in Fig. 2, as computed using the numerical bifurcation software MATCONT [33]. On the range of parameters where the steady-state is linearly unstable, we observe from Fig. 2 the existence of a linearly stable periodic solution.

We remark that when the intracellular kinetics is uncoupled from the bulk, it is well-known for the Sel'kov dynamics (3.3) that Hopf bifurcations are always supercritical (cf. [34]). By coupling the intracellular kinetics linearly via the global mode U_0, we observe from Fig. 2 that supercritical Hopf bifurcations still occur.

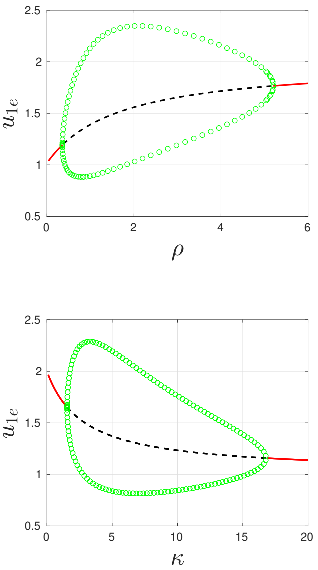

Figure 2: Global bifurcation diagrams for the ODE system (3.2) showing steady-states and branches of periodic solutions for $m = 6$ identical cells, as computed using MATCONT [33], for the Sel'kov kinetics (3.3) with parameters in (3.13) and with $D_0 = 0.5$. Top panel: For $\kappa = 3.2$, the HB points occur at $\rho_1 = 0.3548$ and $\rho_2 = 5.2035$. Right panel: For the unit sphere where $\rho = 1.4324$, the HB points occur at $\kappa_1 = 1.5508$ and $\kappa_2 = 16.7814$. The red-solid and black-dashed lines represent linearly stable and unstable branches, respectively. The green loop represents linearly stable branches of periodic solutions.

From Fig. 2 we observe that there are no intracellular oscillations when either κ is sufficiently small or large. Since κ is the dimensionless ratio of the decay rate k_B of the bulk species to the reaction rate k_R of the local kinetics of the cells (see (1.3)), a small value of κ implies that the rate of intracellular reactions is relatively high compared to the decay rate of the bulk species. As a result, the intracellular dynamics tend quickly to the quiescent state since the Sel'kov parameters are chosen so that the steady-state for each cell is linearly stable when isolated. Alternatively, a large value of κ implies that the secreted intracellular species has a short length-scale for decay in the bulk region, making it difficult to have the strong inter-cellular communication that is needed for collective oscillations or quorum-sensing behavior.

In Fig. 3, we show numerical results computed from the ODE system (3.2) using *ODE45* in MATLAB [35] for $m = 6$ identical cells in the unit sphere where $\rho = 1.4324$, with parameters in (3.13), and with $D_0 = 0.5$. In the top panel of Fig. 3, where $\kappa = 1$, we observe damped intracellular oscillations leading to a linearly stable steady-state as predicted by the bifurcation diagram in the bottom panel of Fig. 2. In contrast, for $\kappa = 3.2$, in the middle and bottom panels of Fig. 3 we observe sustained oscillations that are triggered by the global coupling. This is consistent with the prediction in Fig. 2 of a stable periodic solution for $\kappa = 3.2$.

3.2. *Quorum sensing and phase synchronization*

To numerically study phase synchronization and dynamical quorum-sensing transitions, we will compute solutions to the ODE system (3.1) and monitor a time-averaged Kuramoto order type parameter in the form introduced originally in [36] given by

$$R = \left\langle \left| N^{-1} \sum_{j=1}^{N} \exp[i\theta_j(t)] - \left\langle N^{-1} \sum_{j=1}^{N} \exp[i\theta_j(t)] \right\rangle \right| \right\rangle , \tag{3.14}$$

where N is the number of oscillators, $\theta_j(t)$ is the instantaneous phase of the j^{th} oscillator, and $\langle \ldots \rangle$ represents average over time. In this form, this order parameter has been used previously in [37] to study phase synchronization for glycolytic oscillations in suspensions of yeast cells and in [14] to quantify the degree of synchronization of chemical oscillations of porous catalytic particles suspended in a Belousov-Zhabotinsky (BZ) reaction mixture. This order parameter has also been used to measure the degree of phase synchrony of coupled non-linear chaotic oscillators [22, 21]. The value of R ranges from 0 to 1, and measures the level of phase synchronization of the oscillators. When $R = 1$, the oscillators are perfectly in phase, and they are perfectly out of phase when $R = 0$.

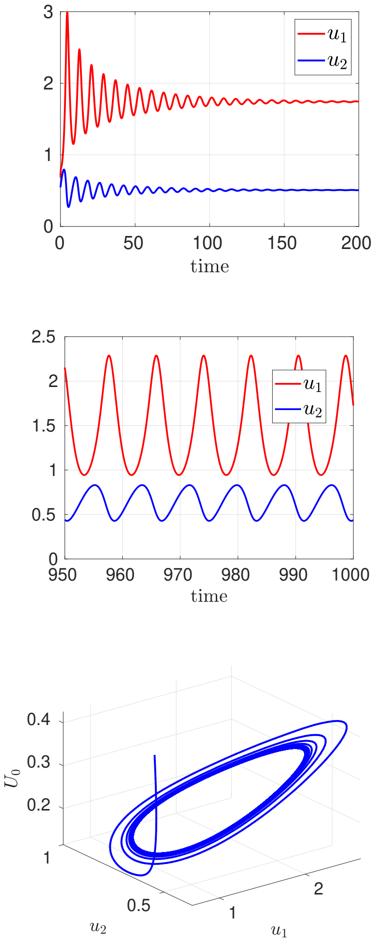

Figure 3: Numerical results for the ODE system (3.2) *showing the intracellular dynamics for $m = 6$ identical cells in the unit sphere, where $\rho = 1.43239$, for Sel'kov kinetics* (3.3)*, with parameters in* (3.13) *and with $D_0 = 0.5$. Top panel: For $\kappa = 1$, damped oscillations occur. Middle panel: For $\kappa = 3.2$, there are sustained oscillations. Bottom panel: 3-D plot for (U_0, u^1, u^2) showing sustained oscillations when $\kappa = 3.2$. Results are consistent with the bifurcation diagram in the bottom panel of Fig. 2.*

To compute R we first solve the ODEs (3.1) with random initial conditions numerically using *ODE45* in MATLAB [35]. After discarding the solution over the transient period, we fit a single-mode Fourier series expansion to one of the solution components for each cell and compute the instantaneous phase $\theta_j(t)$ from the coefficients of the series, from which we calculate the phase average $z = N^{-1} \sum_{j=1}^{N} e^{i\theta_j}$. Next, we compute an average of the instantaneous averages $\langle z \rangle$ over a specified time interval (after the system has reached a quasi steady-state). The modulus of the difference between the instantaneous averages z and the time-average $\langle z \rangle$ is computed for each time point, and the corresponding result averaged over time to obtain the order parameter R, as given in (3.14). In our computations, we set $R = 0$ when the cells are in a quiescent state or when the amplitude of the oscillations is less than 1×10^{-4}.

In our examples below, the cell population $m = 1000$ is fixed and will be taken to be a mixture of identical and *defective* cells, where the heterogeneous cells have a different Sel'kov kinetic parameter α in (3.3). Since $\rho \equiv m/|\Omega|$ and m is fixed, a change in ρ represents a change in the domain volume $|\Omega|$. In Fig. 4 we plot the order parameter R and the amplitude of oscillation for 1000 identical cells versus ρ. We observe that there are no oscillations when ρ is small and that there is a sudden switch-like transition to perfect phase synchronization when $\rho \approx 0.36$. This phase synchrony is maintained until $\rho \approx 5.28$ where there is a further switch-like transition that leads to oscillator death and a quiescent state.

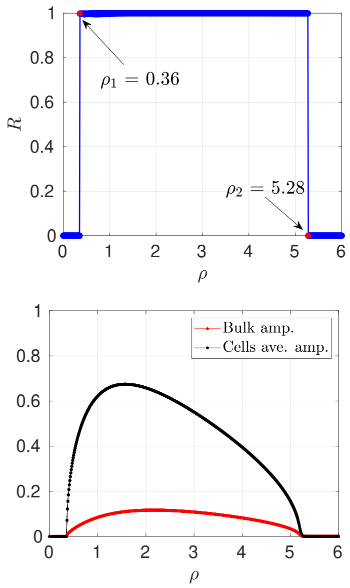

Figure 4: The degree of phase synchronization and amplitude of oscillation for 1000 identical cells, computed from the ODEs (3.1) with Sel'kov kinetics (3.3), parameters in (3.13), and with $D_0 = 0.5$ and $\kappa = 3.2$. Top panel: The Kuramoto order parameter R in (3.14) versus the cell density parameter ρ. Synchronous oscillations are triggered at $\rho_1 = 0.36$ and extinguished at $\rho_2 = 5.28$. Bottom panel: The average amplitude of oscillation in the cells (black) and in the bulk region (red) versus ρ.

To qualitatively interpret this behavior, there are no synchronous intracellular oscillations when ρ is small since the domain is too large for them to communicate effectively through the diffusing bulk signal. As ρ increases, the domain volume shrinks, thereby bringing the cells closer together and ultimately leading to synchronous oscillations and quorum-sensing behavior. However, as ρ continues to increase, the synchronous oscillations are quenched because the cells become more tightly packed, with a smaller bulk region, and so effectively behave like a single giant cell. Since the Sel'kov parameters (3.13) are chosen so that the steady-state of an individual cell is linearly stable when isolated from the bulk, the steady-state for the giant cell is also stable.

To further elucidate the mechanism for the quenching of oscillations shown in Fig. 4 when ρ exceeds a threshold, we first observe from (3.4) that $u_e^1 \equiv v_e \to \mu$, $u_e^2 \equiv w_e \to \mu/(\alpha+\mu^2)$ and $U_{0e} \to \mu k_2/k_1$ as $\rho \to \infty$. As a result, for $\rho \gg 1$, we have that $\text{tr}(J_e) = 2 w_e v_e - 1 - \epsilon_0(\alpha + v_e^2) < 0$ since the reaction-kinetic parameters are chosen so that an isolated cell, which is uncoupled from the bulk, has a linearly stable steady-state. Therefore, for the polynomial (3.9) we have from (3.10) that for $\rho \gg 1$

$$\begin{aligned} &q_1 \sim \rho k_1 = \mathcal{O}(\rho)\,, \quad q_1 q_2 \sim \rho^2 k_1^2 |\text{tr}(J_e)| = \mathcal{O}(\rho^2)\,, \\ &q_3 \sim \rho k_1 \det(J_e) = \mathcal{O}(\rho)\,, \quad \to \quad q_1 q_2 \gg q_3\,, \end{aligned} \tag{3.15}$$

which shows that the Routh-Hurwitz linear stability criterion (3.11) is satisfied for $\rho \gg 1$. Therefore, for ρ sufficiently large the steady-state is linearly stable. This analysis suggests that there is a critical value ρ_m of the cell density parameter ρ, with ρ_m sufficiently large, for which the steady-state of (3.2) is linearly stable when $\rho > \rho_m$ (see the upper threshold in Fig. 4).

In Fig. 5, we present similar results for 500 identical and 500 *defective* cells. The identical cells have parameters in (3.13), while for the defective cells the Sel'kov kinetic parameter α is selected uniformly from the interval $0.92 < \alpha < 0.95$. From Fig. 5, we observe that synchronous oscillations are triggered at $\rho = 0.44$ and quenched at $\rho = 4.49$, which provides (as expected) a smaller range of ρ where phase synchrony occurs as compared to the case of 1000 identical cells. For 200 identical and 800 defective cells, in Fig. 6 we show that the range in ρ where perfect phase synchrony occurs is further decreased as compared to that in Fig. 5.

In summary, we conclude from Figs. 4–6 that the cell population density plays a dual role of both triggering and quenching synchronous intracellular oscillations. When it triggers oscillations, it does so through quorum sensing. This is similar to the result obtained in Section 4.2 of [24]. Moreover, as the percentage of defective cells in the population increases, the range of ρ for which synchronous oscillations are predicted decreases, as does the amplitude of intracellular and bulk

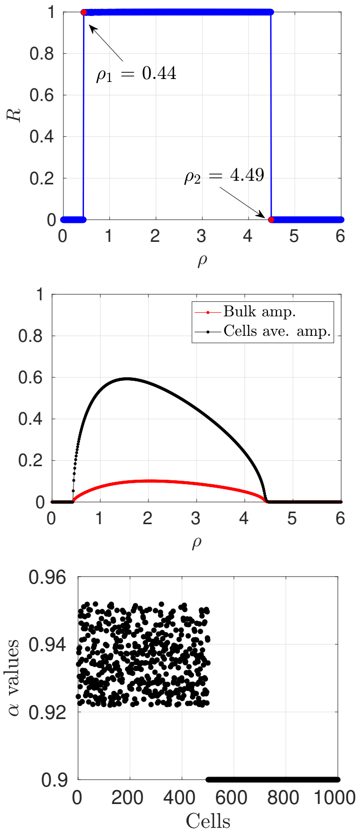

Figure 5: The degree of phase synchronization and amplitude of oscillation for 500 identical and 500 defective cells, computed from the ODEs (3.1) for Sel'kov kinetics (3.3) with $D_0 = 0.5$ *and* $\kappa = 3.2$. *The identical cells have parameters in (3.13). The kinetic parameter* α *for the defective cells are selected uniformly from the interval* $0.92 < \alpha < 0.95$, *with* $\alpha = 0.9$ *for the identical cells. Top panel: The Kuramoto order parameter (3.14) with respect to* ρ. *Phase synchronization is triggered at* $\rho_1 = 0.44$ *and extinguished at* $\rho_2 = 4.49$. *Middle panel: The average amplitude of oscillation in the cells (black) and in the bulk region (red) with respect to* ρ. *Bottom panel: Values of* α *for the 1000 cells.*

oscillations. Overall, Figs. 4–6 indicate for our leading-order system (3.1) that effective communication leading to synchronous intracellular oscillations is more difficult to achieve among a population of non-identical cells.

4. Effect of location on intracellular dynamics

Within the unit sphere, we now examine the effect on the intracellular dynamics of including the $O(\varepsilon)$ correction terms in the ODEs (2.18) that incorporates the spatial configuration of the cells. In order to clearly illustrate quorum-sensing and diffusion-mediated communication through the aid of global bifurcation diagrams we will focus our case study below to a small population of $m = 6$ cells.

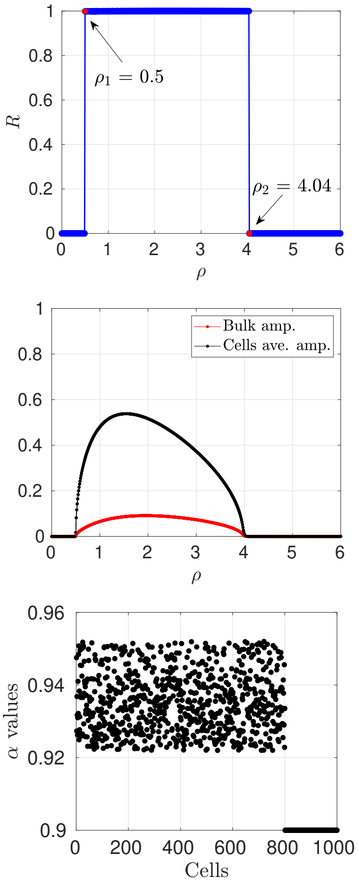

Figure 6: Same caption as in Fig. 5 except that there are now 200 identical and 800 defective coupled cells. Synchronous oscillations are now triggered at $\rho_1 = 0.5$ *and extinguished at* $\rho_2 = 4.04$.

The effect of cell location is encoded by the Neumann Green's function satisfying (2.10), which is given for the unit sphere by (cf. [38])

$$G(\mathbf{x};\mathbf{x}_j) = \frac{1}{4\pi|\mathbf{x}-\mathbf{x}_j|} + \frac{1}{4\pi|\mathbf{x}||\mathbf{x}'-\mathbf{x}_j|} + \frac{(|\mathbf{x}|^2 + |\mathbf{x}_j|^2)}{6|\Omega|} + \frac{1}{4\pi}\log\left(\frac{2}{1-\mathbf{x}\cdot\mathbf{x}_j + |\mathbf{x}||\mathbf{x}'-\mathbf{x}_j|}\right) - \frac{7}{10\pi}\,, \tag{4.1a}$$

where the regular part of G is given by

$$R_j \equiv R(\mathbf{x}_j) = \frac{1}{4\pi\left(1-|\mathbf{x}_j|^2\right)} + \frac{1}{4\pi}\log\left(\frac{1}{1-|\mathbf{x}_j|^2}\right), + \frac{|\mathbf{x}_j|^2}{4\pi} - \frac{7}{10\pi}\,, \tag{4.1b}$$

In (4.1), $|\Omega| = 4\pi/3$ and $\mathbf{x}' = \mathbf{x}/|\mathbf{x}|^2$ is the image point to $\mathbf{x}$ outside the sphere. With this explicit result, the Neumann Green's matrix $\mathcal{G}$ in (2.13) can be readily evaluated. Below we will consider three specific cell configurations within the unit sphere: symmetrically located cells on the surface of a concentric sphere, arbitrarily located cells on the surface of a concentric sphere, and arbitrarily located cells within the unit sphere.

4.1. Symmetrically located cells on a concentric sphere

We consider $m = 6$ identical cells of a common radius ε, symmetrically located on the surface of a concentric sphere of radius r_0 with $0 < r_0 < 1$, such as illustrated in Fig. 7 when $r_0 = 0.5$.

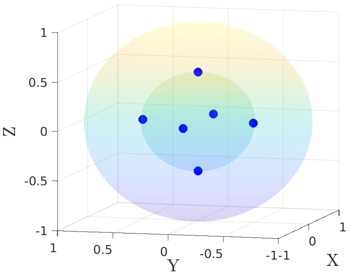

Figure 7: A configuration of six symmetrically located cells (in blue) on the surface of a concentric sphere of radius $r_0 = 0.5$ within the unit sphere. The cell locations are: $(r_0, 0, 0)$, $(-r_0, 0, 0)$, $(0, r_0, 0)$, $(0, -r_0, 0)$, $(0, 0, r_0)$ and $(0, 0, -r_0)$.

For this cell configuration, the Neumann Green's matrix $\mathcal{G}$ is symmetric and cyclic, so that it has the eigenpair

$$\mathcal{G}\mathbf{e} = \sigma\mathbf{e}\,; \quad \mathbf{e} \equiv (1, \ldots, 1)^T\,, \quad \sigma = R_1 + \sum_{j=2}^{m} G(\mathbf{x}_1; \mathbf{x}_j)\,. \tag{4.2}$$

Here, $\sigma \equiv \sigma(r_0)$, where r_0 is the distance from the origin to the radius of the sphere on which the cells are located.

As a result, for identical cells with this configuration we seek a solution to (2.18) where $\mathbf{u}_j = \mathbf{u} = (u^1, u^2)^T$ for $j = 1, \ldots, m$. Upon using $\mathbf{e}^T\mathcal{G}\,\mathbf{e} = m\sigma$, we readily derive that (2.18) reduces to

$$\begin{aligned} U_0' &= -\kappa U_0 - \rho\Big(k_1 U_0 - k_2 u^1\Big) - 4\pi\varepsilon\rho\widetilde{c}k_1\sigma\,, \\ \frac{d\mathbf{u}}{dt} &= \mathbf{F}(\mathbf{u}) + \mathbf{e}_1\Big(k_1 U_0 - k_2 u^1\Big) + 4\pi\varepsilon\widetilde{c}k_1\sigma\mathbf{e}_1\,, \end{aligned} \tag{4.3}$$

where $\mathbf{e}_1 \equiv (1, 0)^T$. Here $\rho = m/|\Omega|$ is the cell density parameter while k_1, k_2, and $\widetilde{c}$ are given by

$$\begin{aligned} k_1 &\equiv \frac{4\pi D_0\widetilde{d_1}}{\widetilde{d_1} + D_0}\,, \qquad k_2 \equiv \frac{4\pi D_0 d_2}{\widetilde{d_1} + D_0}\,, \\ \widetilde{c} &\equiv \frac{1}{4\pi D_0}(k_2 u^1 - k_1 U_0)\,. \end{aligned} \tag{4.4}$$

By substituting $\widetilde{c}$ from (4.4) into (4.3), we obtain a three-component ODE system for (U_0, u^1, u^2) given by

$$\begin{aligned} U_0' &= -(\kappa + \rho\chi)\,U_0 + \rho\xi u^1\,, \\ \frac{d\mathbf{u}}{dt} &= \mathbf{F}(\mathbf{u}) + \Big(\chi U_0 - \xi u^1\Big)\,\mathbf{e}_1\,, \end{aligned} \tag{4.5}$$

where the newly introduced parameters $\chi \equiv \chi(r_0)$ and $\xi \equiv \xi(r_0)$ are defined in terms of $\varepsilon\sigma(r_0)/D$ by

$$\chi \equiv k_1 - \frac{\varepsilon\sigma}{D_0}k_1^2\,, \qquad \xi \equiv k_2 - \frac{\varepsilon\sigma}{D_0}k_1 k_2\,. \tag{4.6}$$

The ODEs (4.5) have a similar structure to the ODE system in (3.2). As such we now perform a HB analysis on (4.5) following the approach used in §3.1. With Sel'kov kinetics (3.3), the steady-state of (4.5) is

$$\begin{aligned} u_e^1 &= \frac{\mu\,(\kappa + \chi\rho)}{(\kappa(1 + \xi) + \rho\chi)}\,, \quad u_e^2 = \frac{\mu}{(\alpha + (u_e^1)^2)}\,, \\ U_{0e} &= \frac{\mu\rho\xi}{(\kappa(1 + \xi) + \rho\chi)}\,. \end{aligned} \tag{4.7}$$

Next, we introduce a perturbation of the steady-state as

$$U = U_{0e} + e^{\lambda t}\eta\,, \qquad \mathbf{u} = \mathbf{u}_e + e^{\lambda t}\phi\,, \tag{4.8}$$

where $\eta \ll 1$ and $\phi \equiv (\phi_1, \phi_2)^T \ll 1$. Upon substituting (4.8) into (4.5), we write the linearized system in matrix form as

$$\mathcal{M}(\lambda)\mathbf{\Psi} = \mathbf{0}\,, \tag{4.9}$$

where $\mathbf{\Psi} \equiv (\eta, \phi_1, \phi_2)^T$ and $\mathcal{M}(\lambda)$ is the 3×3 matrix

$$\mathcal{M}(\lambda) \equiv \begin{pmatrix} -(\kappa + \rho\chi) - \lambda & \rho\xi & 0 \\ \chi & (f_v^e - \xi - \lambda) & f_w^e \\ 0 & g_v^e & (g_w^e - \lambda) \end{pmatrix}. \tag{4.10}$$

Here, $(v, w)^T \equiv (u^1, u^2)^T$, f_v^e, f_w^e, g_v^e and g_w^e are the partials of $f(v, w)$ or $g(v, w)$ evaluated at the steady-state $\mathbf{u}_e = (v_e, w_e)^T$. The characteristic polynomial for λ is

$$\lambda^3 + \gamma_1\lambda^2 + \gamma_2\lambda + \gamma_3 = 0\,, \tag{4.11}$$

with coefficients given by

$$\begin{aligned} \gamma_1 &= (\kappa + \xi + \rho\chi) - \text{tr}(J_e)\,, \\ \gamma_2 &= \det(J_e) - (\kappa + \rho\chi)\,\text{tr}(J_e) + \xi\,(\kappa - g_w^e)\,, \\ \gamma_3 &= (\kappa + \rho\chi)\det(J_e) - \kappa\xi g_w^e\,, \end{aligned} \tag{4.12}$$

where $\det(J_e) = \epsilon_0(\alpha + v_e^2) > 0$ and $\operatorname{tr}(J_e) = 2w_e v_e - 1 - \epsilon_0(\alpha + v_e^2)$ are the determinant and trace of the Jacobian matrix J_e of the Sel'kov kinetics evaluated at the steady-state $\mathbf{u}_e$. Similar to the analysis in §3.1, we conclude by the Routh-Hurwitz criterion that a HB point for the linearization must satisfy

$$\gamma_1 > 0\,, \quad \gamma_3 > 0\,, \quad \text{and} \quad \gamma_1\gamma_2 = \gamma_3\,. \tag{4.13}$$

This HB criterion is used below to determine how the triggering of oscillatory instabilities depends on D_0 and r_0. Global branches of steady-state and periodic solutions for (4.5) are computed using MATCONT [33].

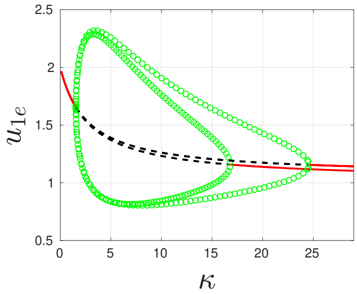

Figure 8: Global bifurcation diagrams for the ODE system (4.5) versus the bulk decay rate κ showing branches of steady-states and periodic solutions computed using MATCONT [33] for $m = 6$ identical cells, with parameters in (3.13) and with $\rho = 1.43239$ and $D_0 = 0.5$. The outer loop is for cells of radius $\varepsilon = 0.05$, symmetrically-spaced on a concentric sphere of radius $r_0 = 0.25$ within the unit sphere, with locations given in the caption of Fig. 7. The HB bifurcation points are $\kappa_1 = 1.5518$ and $\kappa_2 = 24.5774$. The inner loop is for the leading-order dynamics (3.2) when $\varepsilon = 0$ (same as bottom panel of Fig. 2), where HB bifurcations occur at $\kappa_1 = 1.551$ and $\kappa_2 = 16.7814$. The red-solid and black-dashed lines represent linearly stable and unstable steady-state branches, respectively. The green loops represent linearly stable branches of periodic solutions.

In Fig. 8 we plot a global bifurcation diagram for the ODE system (4.5) versus the bulk decay rate κ for $D_0 = 0.5$, $\rho = 1.4324$, and for $m = 6$ symmetrically-spaced identical cells on a ring of radius $r_0 = 0.25$ with a cell radius $\varepsilon = 0.05$. The Sel'kov parameters and permeabilities are as in (3.13). In this figure, we have overlayed the corresponding bifurcation diagram shown in the bottom panel of Fig. 2 that was based on the leading-order dynamics (3.2) when $\varepsilon = 0$. From Fig. 8 we observe that there are values of κ for which linearly stable periodic solutions exist for the symmetric cells but not for the leading-order dynamics. The existence of this significantly larger upper range of κ where periodic solutions can occur is attributed to the fact that $r_0 = 0.25$ is rather small, and so the cells are still able to readily communicate through the bulk diffusion field even when there is a stronger decay of the bulk signal. Overall, Fig. 8 shows clearly that the inclusion of the $O(\varepsilon)$ terms in the ODEs (4.5), incorporating the effect of weak spatial heterogeneity, can be a significant factor in determining whether or not intracellular oscillations can occur.

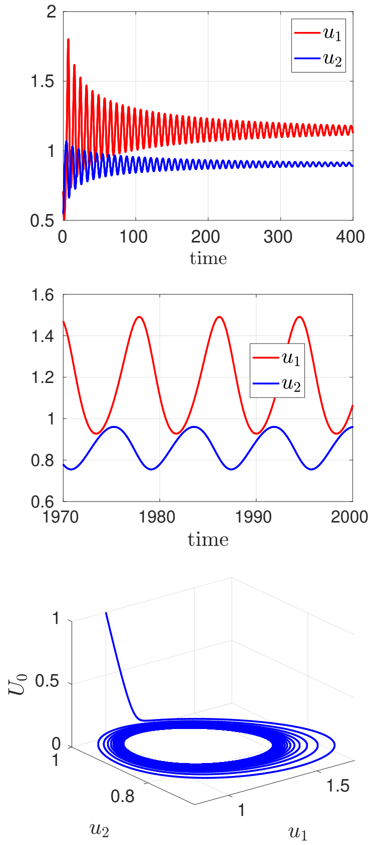

Figure 9: Numerical simulation of ODE dynamics using ODE45 in MATLAB for the parameters in the caption of Fig. 8 with $\kappa = 18.5$. Top panel: For the leading-order dynamics (3.2) there is a slow decay to the linearly stable steady-state. Middle panel: For (4.5) with symmetrically-spaced cells with ring radius $r_0 = 0.25$ and cell radius $\varepsilon = 0.05$, there are sustained intracellular oscillations. Bottom panel: 3-D plot showing the sustained oscillatory dynamics in the middle panel with respect to the three variables.

In Fig. 9 we confirm the predictions of the global bifurcation diagram in Fig. 8. For $\kappa = 18.5$, the intracellular dynamics are predicted to have a linearly stable steady-state for the leading-order dynamics (3.2). In contrast, for this same value of κ, synchronous intracellular oscillations are predicted for (4.5) when the $O(\varepsilon)$ spatial effects are included. These two predictions are confirmed from the ODE dynamics shown in the top and middle panels of Fig. 9. In the bottom panel of Fig. 9 we show a 3-D plot of the sustained oscillation for (4.5), which shows that the amplitude of bulk oscillations is rather small as compared to those in the cells.

In the top panel of Fig. 10 we study the effect on the global bifurcation diagrams for (4.5) of varying the ring radius r_0 for $m = 6$ symmetrically-spaced cells. The remaining parameters are as in the caption of Fig. 8. From this figure, we observe that the smallest range of the bulk decay parameter κ for which intracellular oscillations are predicted is for $r_0 = 0.5$, followed by $r_0 = 0.85$, and then $r_0 = 0.25$. When $r_0 = 0.5$, the cells are far from each other and from the domain boundary, so that it is more difficult to trigger synchronous oscillations through the bulk medium than for $r_0 = 0.25$. For $r_0 = 0.85$, although the cells are far from each other, each cell is relatively close to an "image" cell through the reflecting boundary of the domain, resulting in a pairwise intracellular communication. In the bottom panel of Fig. 10, we plot the two HB points in κ versus r_0, as computed using two-parameter continuation in MATCONT [33] (solid black curves) and from the HB criteria in (4.13) (blue dots). In this figure, linearly stable periodic solutions exist in the region between the two black curves. For $\varepsilon = 0.05$, we observe that the smaller HB value of κ is rather insensitive to r_0 provided that $2\varepsilon = 0.1 < r_0 < 1 - 2\varepsilon = 0.9$. Since the asymptotic theory leading to the ODEs (4.5) is valid only for well-separated cells, we require $\mathcal{O}(\varepsilon) \ll r_0 \ll 1 - \mathcal{O}(\varepsilon)$. From the bottom panel of Fig. 10, the smallest range of κ where periodic solutions occur is when $r_0 = 0.6$, with HB points at $\kappa_1 \approx 1.55$ and $\kappa_2 \approx 13.7$.

Fig. 11 shows the time-dynamics of the ODEs (4.5) for three pairs of (r_0, κ) and with remaining parameter values as in the caption of Fig. 10. The dynamics shown agree with the results predicted from the global bifurcation diagrams in Fig. 10.

Next, we investigate the effect of the bulk diffusivity D_0 on the dynamics. In the top panel Fig. 12 we plot the global bifurcation diagram for (4.5) versus D_0 for two values of ε when $r_0 = 0.25$ and $\kappa = 18.5$. When accounting for a finite cell radius, we observe that the range of D_0 where oscillations are predicted is larger than for the leading-order ODE system (3.2) where $\varepsilon = 0$. In the bottom panel of Fig. 12 we plot the two HB points in D_0 for each r_0 in $0 < r_0 < 1$ as computed from MATCONT from (4.5) or from our HB criteria (4.13). Linearly stable periodic solutions exist in the region bounded by the black curves. Since our asymptotic theory is valid only when $\mathcal{O}(\varepsilon) \ll r_0 \ll 1 - \mathcal{O}(\varepsilon)$, we neglect the horizontal line near $r_0 = 1$ in the bottom panel of Fig. 12. From this figure, we observe that in the completely well-mixed limit, for which $D_0 \to \infty$, no intracellular oscillations will occur when $0.2 < r_0 < 0.8$, as the bulk signal is washed out. However, for a finite D_0 in some range, intracellular oscillations do occur. We suggest that this can be interpreted as *diffusion-sensing* behavior. For $r_0 = 0.25$ and $\kappa = 18.5$, the time-dynamics computed from (4.5) shown in Fig. 13 confirm the predictions of our bifurcation diagram in the top panel of Fig. 12 for three pairs of (ε, D_0).

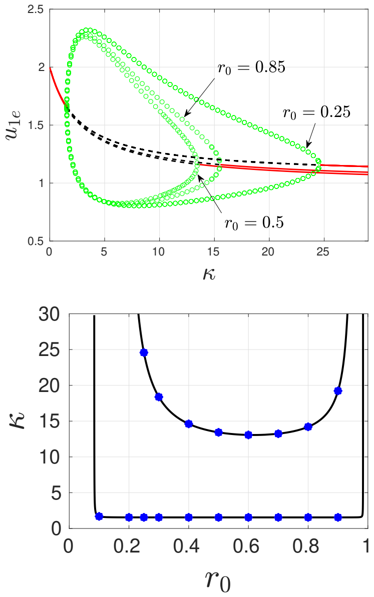

Figure 10: Top panel: Global bifurcation diagrams for the ODE system (4.5) versus κ for three values of ring radii r_0, as computed using MATCONT [33] for $m = 6$ symmetrically-spaced identical cells of radii $\varepsilon = 0.05$, with parameters in (3.13) and with $\rho = 1.43239$ and $D_0 = 0.5$. The HB points are: $\kappa_1 = 1.5518$, $\kappa_2 = 24.577375$ for $r_0 = 0.25$; $\kappa_1 = 1.5504$, $\kappa_2 = 13.5721$ for $r_0 = 0.5$; $\kappa_1 = 1.5506$, $\kappa_2 = 15.5074$ for $r_0 = 0.85$. Bottom panel: Two-parameter HB continuation for κ versus r_0. The black curves are the HB boundaries computed from MATCONT. The blue dots are based on the HB criteria in (4.13). Linearly stable periodic solutions exist in the region between the two black curves. The asymptotic theory is valid only when $\mathcal{O}(\varepsilon) \ll r_0 \ll 1 - \mathcal{O}(\varepsilon)$, and so the vertical lines are not relevant.

4.2. *Arbitrarily located cells on a concentric sphere*

We now consider $m = 6$ identical, but non-equally spaced cells on a concentric ring of radius r_0 within the unit disk. For identical cells, for which $k_{1j} = k_1$ and $k_{2j} = k_2$ for $j = 1, \ldots, m$, the ODE system (2.18) reduces to

$$U_0' = -\kappa U_0 + \frac{\rho}{m} \sum_{j=1}^{m} \left(k_2 u_j^1 - k_1 U_0 \right) \tag{4.14a}$$

$$- \frac{4\pi\rho k_1 \varepsilon}{m} \sum_{j=1}^{m} (\mathcal{G}\mathbf{c})_j \, , \tag{4.14b}$$

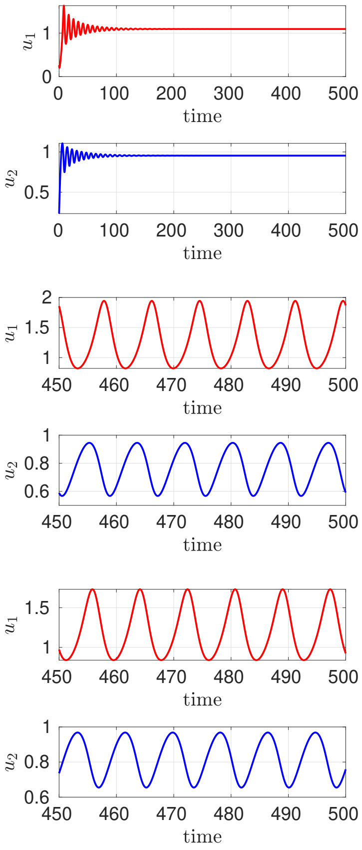

Figure 11: Numerical simulations of ODE dynamics for (4.5) for the parameters in the caption of Fig. 10. Top panels: $r_0 = 0.5$ and $\kappa = 23$ (decaying oscillations). Middle panels: $r_0 = 0.5$ and $\kappa = 7.5$ (sustained oscillations). Bottom panel: $r_0 = 0.25$ and $\kappa = 20$ (sustained oscillations). The results agree with our predictions in the bifurcation diagrams of Fig. 10.

which is coupled to the intracellular dynamics by

$$\frac{d\mathbf{u}_j}{dt} = \mathbf{F}_j\left(\mathbf{u}_j\right) - \mathbf{e}_1\left(k_2 u_j^1 - k_1 U_0\right) + 4\pi k_1 \varepsilon \mathbf{e}_1 (\mathcal{G}\widetilde{\mathbf{c}})_j \,, \tag{4.14c}$$

for $j = 1, \ldots, m$, where $\mathbf{e}_1 = (1,0)^T$, $\rho = m/|\Omega|$ is the cell density parameter, ε is the common radius of the cells, and $\mathcal{G}$ is the Neumann Green's matrix of (2.13), which depends the spatial configuration of the cells. In (4.14), k_1 and k_2 are defined in (4.4), and $\widetilde{c}_j$ is given by

$$\widetilde{c}_j = \frac{1}{4\pi D_0}\left(k_2 u_j^1 - k_1 U_0\right), \quad \widetilde{\mathbf{c}} \equiv (\widetilde{c}_1, \ldots, \widetilde{c}_m)^T \,. \tag{4.14d}$$

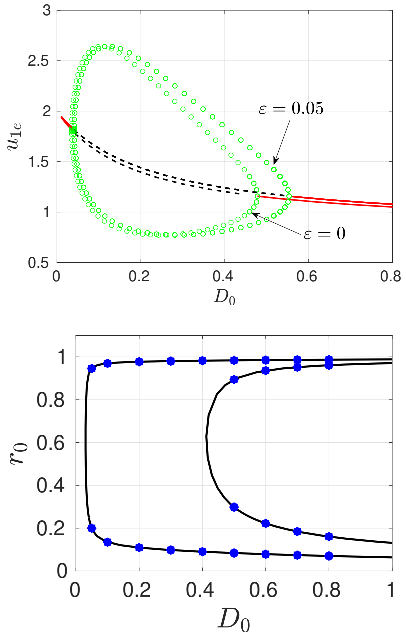

Figure 12: Top panel: Global bifurcation diagrams when $\kappa = 18.5$ and $r_0 = 0.25$ for the ODE system (4.5) versus D_0 for $\varepsilon = 0.05$ and for the leading-order dynamics (3.2) where $\varepsilon = 0$, as computed using MATCONT [33]. The remaining parameters are in (3.13) with $\rho = 1.43239$. The range in D_0 where oscillations occur is larger when $\varepsilon = 0.05$. Bottom panel: Two-parameter HB continuation for D_0 versus r_0 when $\varepsilon = 0.05$. The black curves are the HB boundaries computed with MATCONT, while the blue dots were obtained using the HB criteria in (4.13). Linearly stable periodic solutions exist in the region enclosed by the black curves. The horizontal line near $r_0 = 1$ is not relevant as it signifies the breakdown of the well-separated cell assumption that is required for the derivation of the ODE system.

For $m = 6$, (4.14) is an ODE system of dimension 13. For all the results and figures in the subsection, we use Sel'kov kinetics (3.3) with parameters and permeabilities as in (3.13). The cell centers are given in Table 1 of Appendix B.1. A schematic illustration of the cell configurations for $r_0 = 0.5$ and $r_0 = 0.85$ is shown in Fig. 14. Our goal is to determine the effect on intracellular oscillations of the new arrangement of cells.

In Fig. 15 we compare the global bifurcation diagrams versus κ for the leading-order dynamics, computed using (3.2), with those for either symmetrically- or arbitrarily-spaced cells on a concentric sphere of radius $r_0 = 0.25$ and cell radius $\varepsilon = 0.05$, as computed from either (4.5) or (4.14), respectively. For these three scenarios, we observe that the largest range of κ for which linearly stable periodic solutions exist is for arbitrarily-located cells. This increased range is likely due to the fact that for arbitrarily-spaced cells, there is at least one pair of cells on the surface of the concentric sphere that are closer than when the cells have maximum inter-cell distance, such as is the case for the symmetrically-spaced configuration. Cells that are in closer proximity can trigger intracellular oscillations

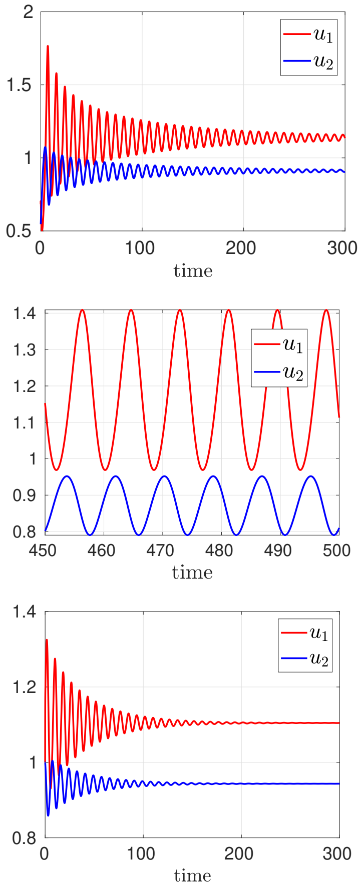

Figure 13: Numerical simulations of ODE dynamics for (4.5) for the parameters in the caption of Fig. 12 with $r_0 = 0.25$ and $\kappa = 18.5$. Top panel: $\varepsilon = 0$ and $D_0 = 0.52$ (decaying oscillations). Middle panel: $\varepsilon = 0.05$ and $D_0 = 0.52$ (sustained oscillations). Bottom panel: $\varepsilon = 0.05$ and $D_0 = 0.7$ (sustained oscillations). The results agree with our predictions in the bifurcation diagrams of Fig. 12.

even when the bulk decay rate κ is rather large. We emphasize that when cells are located on a concentric ring, the effect of the nearest "ghost" cell across the reflecting outer boundary of the sphere is the same for each cell.

In Fig. 16, we show the time-dynamics for the ODE systems (4.5) and (4.14) for a few values of κ that confirm predictions from the bifurcation diagrams of Fig. 15. In this figure, the colors of the curves correspond to the color codes for the cells in Fig. 14 and Table 1. In the top two panels, where $\kappa = 28$, we observe a slow synchronous oscillatory decay to the linearly stable steady-state for the symmetrically-spaced cell configuration. However, when $\kappa = 28$, from the middle two panels in Fig. 16 we observe roughly synchronous intracellular oscillations for the arbitrarily-spaced pattern, Finally, in the bottom two panels, for $\kappa = 36$ and arbitrarily-spaced cells, we observe a slow decay of intracellular oscillations to the linearly stable steady-state.

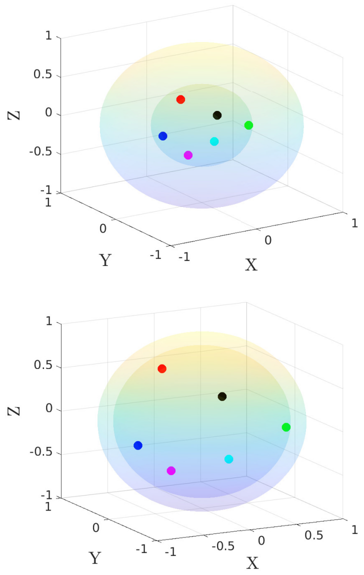

Figure 14: Schematic plot for $m = 6$ identical, but non-equally spaced, cells centered on a concentric sphere of radius $r_0 = 0.5$ (top panel) and $r_0 = 0.85$ (bottom panel) within the unit sphere. The cell centers can be generated from Table 1 of Appendix B.1 for a given r_0. The color codes are for easy referencing.

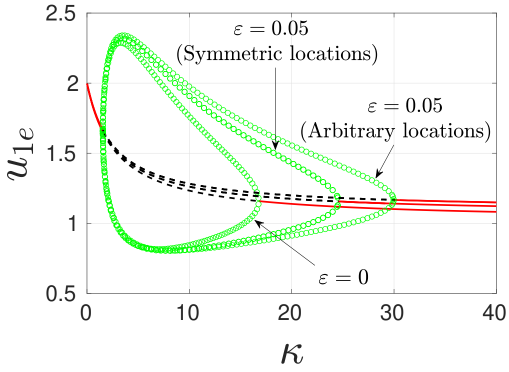

Figure 15: Global bifurcation diagrams versus κ comparing the range where intracellular oscillations occur for either the leading-order dynamics, symmetrically-spaced cells, or arbitrarily-spaced cells, as computed from (3.2), (4.5) and (4.14), respectively, using MATCONT [33]. Parameters as in (3.13) with $\rho = 1.4324$ and $D_0 = 0.5$. The concentric ring has radius $r_0 = 0.25$ and $\varepsilon = 0.05$. The green loops representing periodic solutions for the leading-order dynamics and for symmetrically-spaced cells are as in Fig. 8. For arbitrarily-spaced cells, with cell locations generated from Table 1, the HB points are at $\kappa_1 = 1.5525$ and $\kappa_2 = 29.9604$.

Next, for arbitrarily-spaced cells, we study the effect of the radius r_0 of the concentric sphere on which the cells

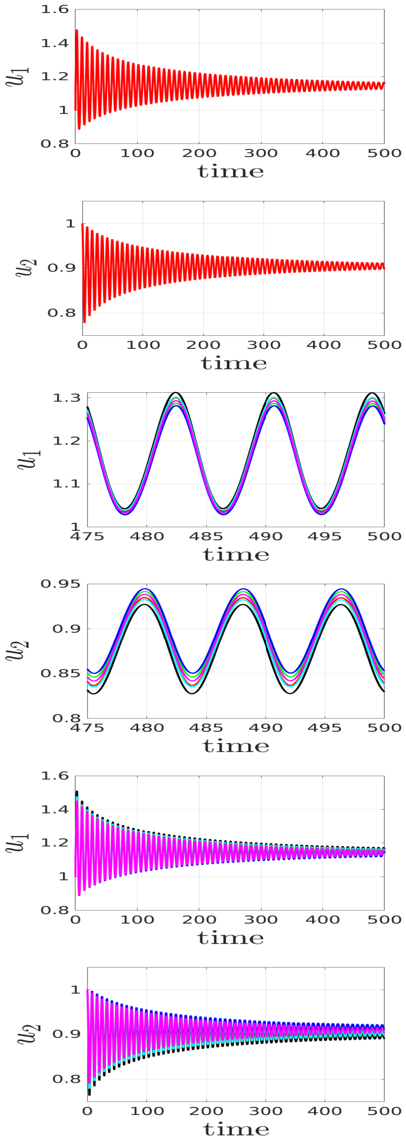

Figure 16: Numerical simulations of ODE dynamics for (4.5) *and* (4.14) *computed using MATLAB for the parameters in the caption of Fig.* 15*. Top two rows: symmetrically-spaced cells with* $\kappa = 28$*, showing decaying oscillations. Middle two rows: arbitrarily-spaced cells with* $\kappa = 28$*, showing sustained and nearly synchronous oscillations. Bottom two rows: The oscillations for arbitrarily-spaced cells now undergo a slow decay to the steady-state when* $\kappa = 36$*. Colors correspond to the color codes for the cells in Fig.* 14 *and Table* 1*.*

are located. The global bifurcation diagrams are shown in the top panel of Fig. 17, while in the bottom panel of Fig. 17 we plot the HB bifurcation points κ versus r_0 using two-parameter continuation. These bifurcation diagrams have a very similar qualitative dependence on r_0 as for the bifurcation plots shown in Fig. 10 for the case where the cells are symmetrically-spaced.

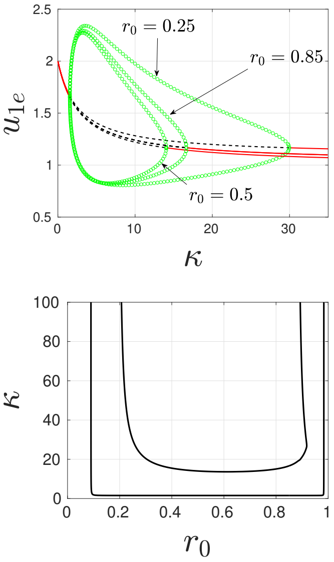

Figure 17: Top panel: Global bifurcation diagrams for the ODE system (4.14) *versus* κ *for three values of ring radii* r_0*, as computed using MATCONT* [33] *for* $m = 6$ *arbitrarily-spaced identical cells on a ring, with locations as generated from Table* 1*, with* $\rho = 1.43239$ *and* $D_0 = 0.5$*. For these values of* r_0*, the largest range of* κ *where intracellular oscillations occur is for* $r_0 = 0.25$*. Bottom panel: Two-parameter HB continuation for* κ *versus* r_0 *computed from MATCONT. Linearly stable periodic solutions exist in the region between the two black curves. The vertical lines are not relevant as they signify the breakdown of the well-separated cell assumption.*

In the global bifurcation diagrams of Fig. 18, we illustrate a qualitatively new behavior that occurs for $r_0 = 0.85$ when we further extend the range of κ. In particular, we observe that there is an additional HB point at $\kappa_3 = 35.0067$. As shown in Fig. 18, linearly stable periodic solutions are predicted when $1.5509 \leq \kappa \leq 16.6489$ and for $\kappa \geq 35.0067$. We emphasize that periodic solutions do not exist for such large values of κ when either $r_0 = 0.25$ and $r_0 = 0.5$.

As a qualitative explanation of the additional HB threshold in Fig. 18, we first observe that when the ring radius is $r_0 = 0.85$ (which is rather close to unity), for each cell on the ring the nearest neighbour is the "ghost" cell that exists on the other side of the domain boundary owing to the reflecting boundary condition. For large κ the bulk signal U_0 is strongly degraded and so effectively only those cells that are spatially close to each other can communicate and trigger oscillations. This pairwise interaction of the ring cells with their "ghost" cells is likely the mechanism underlying the additional branch of periodic solutions shown in Fig. 18 when κ is large.

In Fig. 19 we show results from numerical simulations

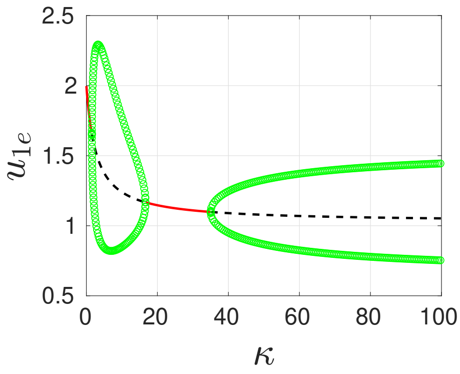

Figure 18: Global bifurcation diagrams for the ODE system (4.14) versus κ, as computed using MATCONT [33] for $m = 6$ arbitrarily-spaced identical cells located on a ring of radius $r_0 = 0.85$, with cell locations generated from Table 1. The remaining parameters are the same as in Fig. 17. There are now three HB bifurcation points at $\kappa_1 = 1.5509$, $\kappa_2 = 16.6489$ and $\kappa_3 = 35.0067$

of the ODE system (4.14) that support the predictions from the global bifurcation diagram in Fig. 18. In particular, in the top two rows where $\kappa = 5$, synchronous oscillations are observed in the entire cell population. In the middle two rows where $\kappa = 25$, damped oscillations occur. However, in the bottom two rows where $\kappa = 45$, we observe that asynchronous intracellular oscillations occur. In particular, the green, cyan, and blue cells synchronize their dynamics, while the red, black and magenta cells also synchronize. However, the dynamics of these two groups of cells are out of phase. We believe that the grouping and synchronization of the cells is based on their spatial proximity, although it is unclear why there only two sub-groups. From Table 2, we observe that the red, black, and magenta cells are closest to each other, while the green, cyan, and blue are also closest to each other. As κ is increased, corresponding to a stronger decay of the bulk signal, the cell-cell distances become an increasingly important factor in determining which cells will synchronize. We remark that for $r_0 = 0.25$ and $r_0 = 0.5$, where all the cells are much more closely spaced, asynchronous oscillations do not occur when $\kappa = 45$.

Lastly, we present global bifurcation diagrams versus D_0 in the top panel of Fig. 20 that compares results for the leading-order dynamics, for symmetrically-spaced cells on a ring of radius $r_0 = 0.25$, and for arbitrarily located cells on a ring of radius $r_0 = 0.25$, as computed from (3.2), (4.5) and (4.14), respectively. We observe that the range of D_0 for which linearly stable periodic solutions exist when the cells are arbitrarily located on the ring is only slightly larger than that of symmetric cells. This is likely due to the closer spatial proximity of some cells in this configuration relative to the symmetric cell pattern. For both configurations, when D_0 is large, the bulk species diffuses away from the cells making it difficult for the cells to communicate. In the bottom panel of Fig. 20, we plot the HB bifurcation curves for r_0 versus D_0 for the arbitrarily-spaced configuration.

4.3. Arbitrarily located cells within the unit sphere

In this subsection we consider $m = 6$ identical cells that are arbitrarily located within the unit sphere, such as shown Fig. 21. The centers of the cells are chosen as in Table 3, and the common cell radius is $\varepsilon = 0.05$. For this cell configuration, we use the ODE system (4.14) to compute global bifurcation diagrams and we will calculate the Kuramoto order parameter (3.14) to study diffusion-mediated synchronization in the cells as D_0 is increased.

For this cell configuration, in Fig. 22 we plot global bifurcation diagrams versus κ (top panel) and versus D_0 (bottom panel) as computed from (4.14) using MATCONT [33]. In the top panel of Fig. 22 where $D_0 = 0.5$, the HB points are $\kappa_1 = 1.5521$ and $\kappa_2 = 15.2509$, while for the bottom panel where $\kappa = 3.2$ the HB occurs when $D_0 = 0.0310$. In this case, we observe that linearly stable periodic solutions exist for all $D_0 \geq 0.0310$.

To further investigate the effect of diffusion on the intracelluar dynamics, in the top panel of Fig. 23 we show numerical results for the Kuramoto order parameter R (3.14) that measures the degree of phase synchronization of intracellular dynamics as D_0 increases. In the bottom panel of Fig. 23 we also show the amplitude of oscillations in the cells and in the bulk region versus D_0. From the top panel of Fig. 23 we observe that there are no intracellular oscillations when $D_0 \leq 0.0301$, but that phase synchronization becomes more evident as D_0 increases past $D_0 = 0.0301$, with almost perfect phase synchronization achieved when $D_0 \approx 0.1$.

These results illustrate *diffusion-mediated synchronization*, where an increase in the diffusion rate of the bulk species increases synchronization in the dynamics of the cells. We now verify our prediction from numerical simulations of the ODE system (4.14) for the cell configuration shown in Fig. 21. The results for u_{j1} are shown in Fig. 24 for $D_0 = 0.02$ (top row), $D_0 = 0.0320$ (second row), $D_0 = 0.0654$ (third row), and $D_0 = 0.1348$ (fourth row). As predicted by the Kuramoto order parameter in Fig. 23, there are no sustained oscillations in the cells for $D_0 = 0.02$. For $D_0 = 0.0320$ (second row), the cells

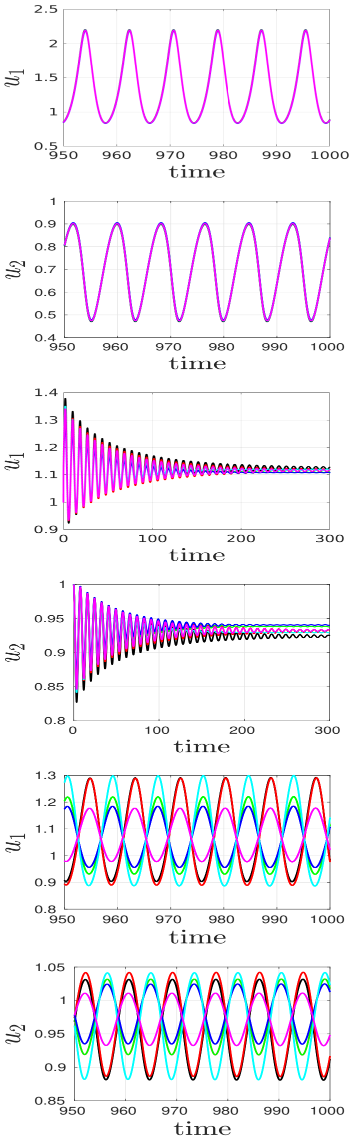

Figure 19: Numerical simulations of ODE dynamics for (4.14) *computed using MATLAB for the parameters in the caption of Fig.* 18 *for arbitrarily-spaced cells on a concentric ring of radius $r_0 = 0.85$ within the unit disk. Top rows: For $\kappa = 5$, sustained synchronous oscillations occur for the entire population. Middle rows: For $\kappa = 25$, decaying oscillations occur. Bottom rows: For $\kappa = 45$, asynchronous oscillations for two groups of cells that are the most closely spaced. The color codes of the trajectories correspond to the color codes for the cells in Fig.* 14*. The cell-cell distances are given in Table* 2*.*

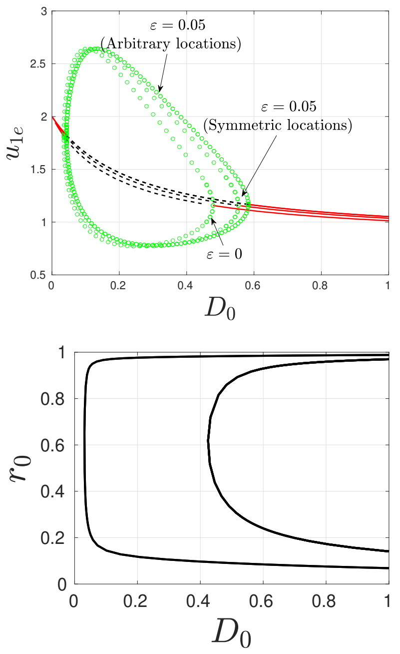

Figure 20: Top panel: Global bifurcation diagrams for the ODE system (4.14) *versus D_0 for $\kappa = 18.5$, comparing results for the leading-order dynamics, for symmetrically-spaced cells on a ring, and for arbitrarily-spaced cells on a ring, as computed using MATCONT* [33]*. The ring radius is $r_0 = 0.25$, and the cell radius is $\varepsilon = 0.05$. Bottom panel: Two-parameter HB continuation for r_0 versus D_0 for arbitrarily-spaced cells on a ring. The horizontal line near $r_0 = 1$ is beyond the range where the well-separated cell assumption is valid.*

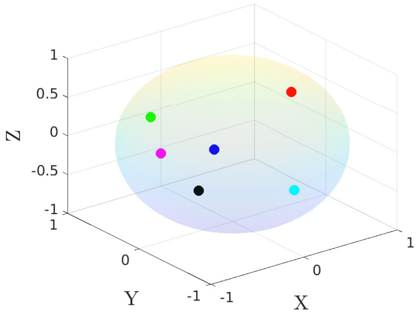

Figure 21: A schematic illustration for $m = 6$ identical cells arbitrarily located within the unit sphere. The centers of the cells are given in Table 3*. The color codes are for easy referencing.*

begin to oscillate with only those that are in close spatial proximity beginning to synchronizing their dynamics, but with small amplitudes. As D_0 increases further, phase synchronization becomes evident as shown in the third row where $D_0 = 0.0654$. The last row of Fig. 24 where $D_0 = 0.1348$ shows perfect phase synchronization in the intracellular dynamics.

5. Instability triggered by a single cell

In this section, we study quorum-sensing (QS) behavior where a single additional cell is able to trigger intracellular oscillations for an entire collection of cells that

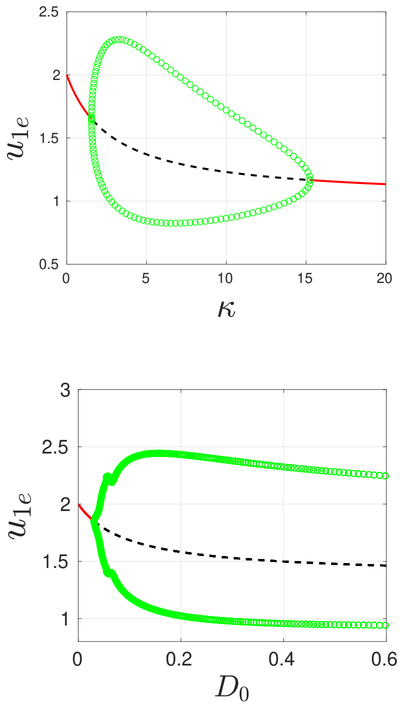

Figure 22: Global bifurcation diagrams versus κ (top panel) or versus D_0 (bottom panel) for the ODE system (4.14) *computed using MATCONT for $m = 6$ identical cells arbitrarily located inside the unit sphere, with cell centers given in Table 3 (see Fig. 21) and with cell radius $\varepsilon = 0.05$. Top panel: For $D_0 = 0.5$, the HB points are at $\kappa_1 = 1.5521$ and $\kappa_2 = 15.2509$. Bottom panel: For $\kappa = 3.2$, the unique HB point is $D_0 = 0.0320$. We predict that intracellular oscillations now occur for all $D_0 > 0.03$, and so will exist in the completely well-mixed regime where $D_0 \to \infty$.*

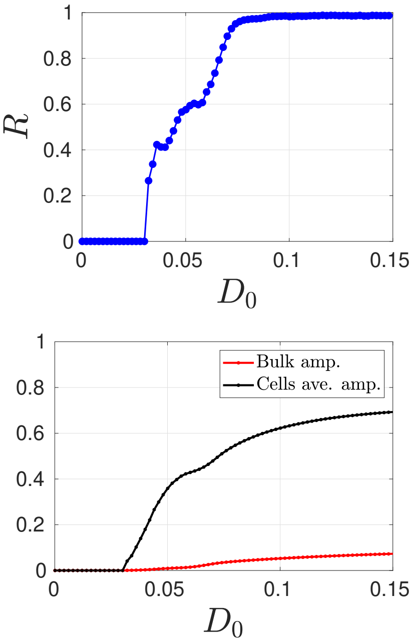

Figure 23: The degree of phase synchronization for $m = 6$ identical cells of radius $\varepsilon = 0.05$ arbitrarily located inside the unit sphere as shown in Fig. 21, computed using the ODEs (4.14) *with $\kappa = 3.2$. Top panel: The Kuramoto order parameter R* (3.14) *versus D_0. Oscillations are triggered at $D_0 \approx 0.0301$ and perfect phase synchronization is achieved at $D_0 \approx 0.1$. Bottom panel: Average amplitude of oscillation in the cells (black) and in the bulk region (red) versus D_0.*

would otherwise be in a quiescent state. For the three configurations of $m = 6$ identical cells in the unit sphere considered in § 4, we introduce an additional cell centered at $(0.75, 0, 0)$ and compare the global bifurcation diagrams for $m = 6$ and $m = 7$ identical cells. To establish QS behavior, we seek parameter regimes where linearly stable periodic solutions exist for $m = 7$ cells, but not for $m = 6$ cells. In contrast to the typical study of QS behavior from ODEs in the well-mixed limit where spatial effects are neglected, our results below shows that the range of κ where QS occurs is dependent on the specific cell configuration used in § 4. The bifurcation results below are computed from the ODE system (2.18) using MATCONT [33] for the Sel'kov parameters in (3.13) and with $\rho = 1.4324$, $D_0 = 0.5$, and $\varepsilon = 0.05$.

We first consider the symmetrically-spaced cell configuration with ring radius $r_0 = 0.5$, where the updated configuration that includes the seventh cell (in orange) is shown in the top row of Fig. 25. In the second row of Fig. 25 we show the global bifurcation diagrams versus the bulk decay rate κ for either $m = 6$ or $m = 7$ identical cells. From this figure, we observe that on the range $13.5721 < \kappa < 16.9869$ collective intracellular oscillations will occur only when the seventh cell is added. To further illustrate this QS behavior, we compute the time-dependent dynamics of $u_{j1}(t)$ from the ODEs (2.18) for $m = 6$ and $m = 7$ cells with $\kappa = 16$, as shown in the third and fourth rows of Fig. 25, respectively. For $m = 6$, we observe, as expected, a slow synchronous decay of the intracellular oscillations to their common steady-state limit. However, by introducing the additional cell, we observe from the fourth row of Fig. 25 sustained, nearly synchronous, intracellular oscillations of different amplitudes. In particular, the cell closest to the seventh (orange) cell is the black cell centered at $(0.5, 0, 0)$. We observe that among all the cells, these two cells have the largest amplitude of oscillations.

A similar result is shown in Fig. 26 for $m = 7$ identical cells, where six of the cells are arbitrarily located

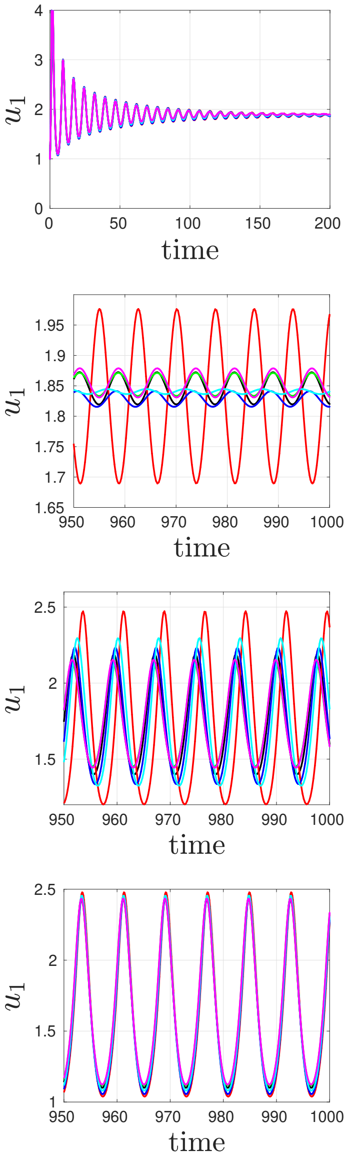

Figure 24: Numerical simulations of the ODE system (4.14) *showing the intracellular species* u_{j1} *as computed using MATLAB for* $m = 6$ *identical cells of radius* $\varepsilon = 0.05$*, arbitrarily located inside the unit sphere as shown in Fig. 21 with* $\kappa = 3.2$*. Row 1:* $D_0 = 0.02$*, Row 2:* $D_0 = 0.0320$*, Row 3:* $D_0 = 0.0654$*, and Row 4:* $D_0 = 0.1348$ *where almost perfect phase synchrony occurs. Colors correspond to the color codes for the cells in Fig. 21.*

on a ring of radius $r_0 = 0.5$, where the coordinates of the cell centers are in Table 1. The cell configuration is shown in the top row of Fig. 26. From the global bifurcation diagrams shown in the second row of Fig. 26, for the range $14.0392 < \kappa < 17.4189$ collective intracellular oscillations will occur only when the seventh cell is added. For $\kappa = 17$, the trajectories for $u_{j1}(t)$ computed from the ODEs (2.18) for $m = 6$ and $m = 7$ cells are shown in the third and fourth rows of Fig. 26, respectively. For this cell configuration, we observe that it is now the green cell that is closest to the seventh (orange) cell. From the fourth row of Fig. 26, we observe that these two cells oscillate in near synchrony and they have the largest amplitudes of oscillation.

Finally, we assume that the six cells are arbitrarily located inside the unit sphere as shown in the top row of Fig. 27. The centers of the first six cells, their distances from the origin, and their center-to-center distances are as in Tables 3 and 4, respectively. Based on the global bifurcation diagrams shown in the second row of Fig. 27, on the range $15.2509 < \kappa < 17.41885$ collective intracellular oscillations will occur only when the seventh cell is added. The numerical results for the trajectories $u_{j1}(t)$ computed from the ODEs (2.18) when $\kappa = 17$, as shown in the third and fourth rows of Fig. 27, confirm this predicted QS behavior. From calculating the sum of the inter-cellular distances in each row of Table 4, we observe that the magenta-colored cell is the one that is on average closest to the other cells. As a result, ignoring the effect of the domain boundary and the image cells outside the domain, which is different for each cell, qualitatively one might expect that this cell will have larger amplitude oscillations than the other cells (see the fourth row of Fig. 27).

Overall, these results show that the inclusion of one single additional cell can, in some parameter range of κ, trigger intracellular oscillations in the entire collection of cells that otherwise would not occur. Moreover, we emphasize that the ranges of κ where this QS behavior will occur depends on the particular spatial configuration of cells. This additional qualitative feature that accounts for the effect of spatial heterogeneity results from the Neumann Green's matrix in (2.18).

6. An integro-differential system for $D = O(1)$

In the limit $\varepsilon \to 0$, we asymptotically reduce (1.2) to derive an integro-differential ODE system for the intracellular dynamics $\mathbf{u}_j(t)$, which is valid when $D = O(1)$. For $D = O(1)$, the limiting bulk diffusion field is no longer approximately spatially homogeneous, and so the previous analysis in §2 is no longer valid. For simplicity, in the analysis below we will assume that the initial conditions are $\mathbf{u}_j(0) = 0$ and that $U(\mathbf{x}, 0) = 0$.

Since there is no initial transient near the cells, we can use the quasi-steady approximation near the cells for all $t > 0$. In this way, for $t = O(1)$, in the j^{th} inner region

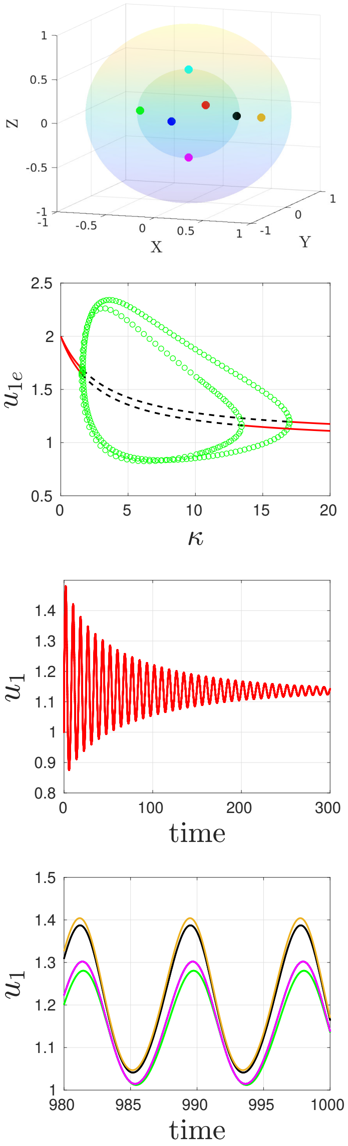

Figure 25: Global bifurcation diagram and numerical results for u_{j1} from the ODE system (2.18) computed using MATLAB for $m = 6$ and $m = 7$ identical cells of radius $\varepsilon = 0.05$ and with $D_0 = 0.5$. Top row: Schematic diagram showing the locations of the cells, where the first six cells are symmetrically placed on a concentric sphere of radius $r_0 = 0.5$ (see Fig. 7 for the centers of the cells) and the seventh cell is located at $(0.75, 0, 0)$. Second row: Global bifurcation diagram for the first six cells only (inner loop) with HB points at $\kappa_1 = 1.5504$ and $\kappa_2 = 13.5721$, and for all the seven cells (outer loop) with HB points at $\kappa_1 = 1.6465$ and $\kappa_2 = 16.9869$. Third Row: Numerical simulations for u_{j1} from the ODE system (2.18) for the first six cells only for $\kappa = 16$, showing decaying oscillations. Bottom row: For $\kappa = 16$, by including the seventh cell, sustained nearly synchronous oscillations will occur. The colors of the trajectories correspond to the color codes for the cells in the top row.

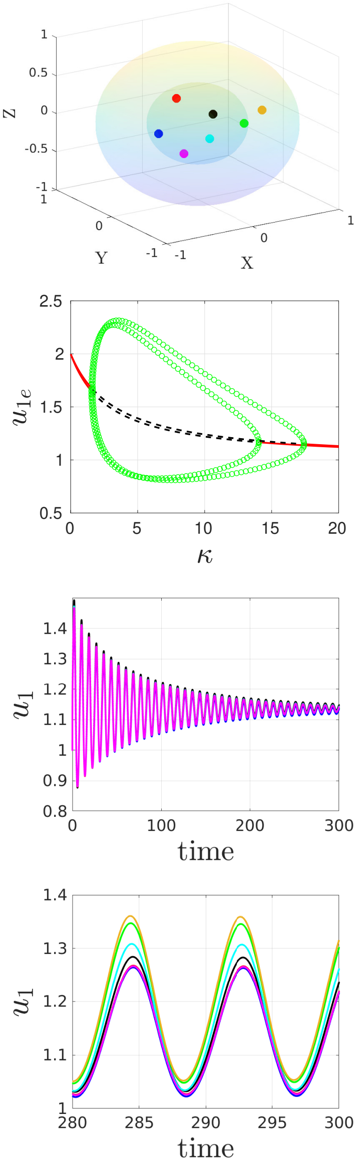

Figure 26: Same caption in Fig. 25 except that the first six cells are arbitrarily-spaced on a concentric sphere of radius $r_0 = 0.5$ (see Table 1 for the centers of the cells), with the seventh cell located at $(0.75, 0, 0)$. Top row: Schematic diagram showing the locations of the cells. Second row: Global bifurcation diagram for the first six cells only (inner loop) with HB points at $\kappa_1 = 1.5504$ and $\kappa_2 = 14.0392$, and for all the seven cells (outer loop) with HB points at $\kappa_1 = 1.6460$ and $\kappa_2 = 17.4189$. Numerical results for $u_{j1}(t)$ from the ODE system (2.18) when $\kappa = 17$ for the first six cells (third row) only and by including the seventh cell (bottom row). We observe that the inclusion of the seventh cell triggers sustained, and nearly synchronous, oscillations in all of the cells. The colors of the trajectories coincide with the color codes of the cells in the top row.

we introduce the local variables $\mathbf{y} = \varepsilon^{-1}(\mathbf{x} - \mathbf{x}_j)$, $r = |\mathbf{y}|$, and $V_j(\mathbf{y}, t) = U(\mathbf{x}_j + \varepsilon\mathbf{y}, t)$. From (1.2a) and (1.2c), we

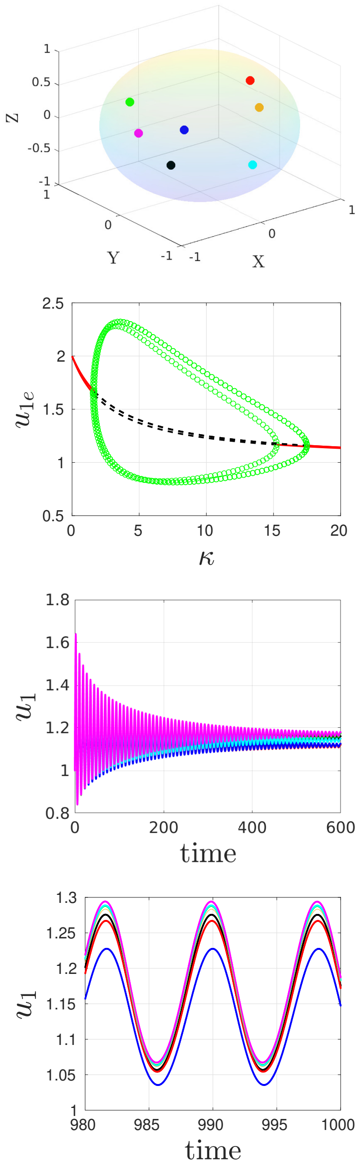

Figure 27: Same caption in Fig. 25 except that the first six cells are arbitrarily spaced within the unit sphere (see Table 3 for the centers of the cells), with the seventh cell located at $(0.75, 0, 0)$*. Top row: Schematic diagram showing the cell locations. Second row: Global bifurcation diagram for the first six cells only (inner loop) with HB points at* $\kappa_1 = 1.5521$ *and* $\kappa_2 = 15.2509$*, and for all the seven cells (outer loop) with HB points at* $\kappa_1 = 1.6453$ *and* $\kappa_2 = 17.4885$*. Numerical results for* $u_{j1}(t)$ *from the ODE system (2.18) when* $\kappa = 17$ *for the first six cells (third row) only and by including the seventh cell (bottom row). Once again, the seventh cell triggers sustained, and nearly synchronous, oscillations in all of the cells. The colors of the trajectories coincide with the color codes of the cells in the top row.*

get the leading-order quasi-steady problem

$$\begin{aligned} &\Delta_r V_j = 0\,, \quad \text{for} \quad r > 1\,, \\ &D\partial_r V_j = d_{1j}V - \frac{d_{2j}}{\varepsilon}u_{j1}\,, \quad \text{on} \quad r = 1\,, \end{aligned} \tag{6.1}$$

which has the radially symmetric solution

$$V(\mathbf{y}, t) = \frac{A_j}{r} + B_j\,, \qquad A_j = \frac{\gamma_j}{4\pi\varepsilon D}\left(u_{j1} - \frac{\varepsilon d_{1j}}{d_{2j}}B_j\right), \tag{6.2}$$

where $A_j \equiv A_j(t, \varepsilon)$, $B_j \equiv B_j(t, \varepsilon)$ and $u_{j1} \equiv u_{j1}(t)$, with initial values $A_j = B_j = u_{j1} = 0$ when $t = 0$. Here γ_j is

$$\gamma_j \equiv \frac{4\pi D d_{2j}}{d_{1j} + D}\,. \tag{6.3}$$

By substituting (6.2) into the intracellular dynamics (1.2d) we obtain the following ODE that is coupled to B_j for each $j = 1, \ldots, m$:

$$\frac{\mathrm{d}\mathbf{u}_j}{\mathrm{d}t} = \mathbf{F}_j\left(\mathbf{u}_j\right) - \gamma_j u_{j1}\mathbf{e}_1 + \frac{\varepsilon d_{1j}}{d_{2j}}\gamma_j B_j(t)\mathbf{e}_1\,. \tag{6.4}$$

To determine $B_j(t)$ we must match the inner solution near the cells to an outer bulk solution. Upon writing (6.2) in outer variables by using $\varepsilon r = |\mathbf{x} - \mathbf{x}_j|$, we obtain that the outer bulk solution $U(\mathbf{x}, t)$ satisfies

$$\begin{aligned} &U_t = D\Delta U - \kappa U\,, \quad \mathbf{x} \in \Omega\backslash\{\mathbf{x}_1, \ldots, \mathbf{x}_m\}\,; \quad U(\mathbf{x}; 0) = 0\,, \\ &U \sim \frac{b_j}{4\pi D}\frac{1}{|\mathbf{x} - \mathbf{x}_j|} + B_j + o(1)\,, \quad \text{as} \quad \mathbf{x} \to \mathbf{x}_j\,, \quad j = 1, \ldots, m\,, \\ &\partial_n U = 0\,, \quad \mathbf{x} \in \partial\Omega\,, \end{aligned} \tag{6.5a}$$

where we have defined

$$b_j(t) \equiv \gamma_j u_{j1}(t) - \frac{\varepsilon\gamma_j d_{1j}}{d_{2j}}B_j(t)\,. \tag{6.5b}$$

To solve (6.5), we first take the Laplace transform to derive that $\hat{U}(\mathbf{x}, s) = \mathcal{L}\left[U(\mathbf{x}, t\right]$ satisfies

$$\begin{aligned} &\Delta\hat{U} - \frac{(\kappa + s)}{D}\hat{U} = -\sum_{k=1}^{m}\frac{\hat{b}_k}{D}\delta(\mathbf{x} - \mathbf{x}_k)\,, \qquad \mathbf{x} \in \Omega\,, \\ &\hat{U} \sim \frac{\hat{b}_j}{4\pi D}\frac{1}{|\mathbf{x} - \mathbf{x}_j|} + \hat{B}_j\,, \quad \text{as} \quad \mathbf{x} \to \mathbf{x}_j\,, \quad j = 1, \ldots, m\,, \\ &\partial_n\hat{U} = 0\,, \quad \mathbf{x} \in \partial\Omega\,, \end{aligned} \tag{6.6}$$

where $\hat{b}_j = \mathcal{L}\left[b_j(t)\right]$ and $\hat{B}_j = \mathcal{L}\left[B_j(t)\right]$.

Next, we decompose (6.6) by writing

$$\hat{U}(\mathbf{x}, s) = \sum_{k=1}^{m}\frac{\hat{b}_k}{D}\hat{G}(\mathbf{x}, s; \mathbf{x}_k)\,, \tag{6.7}$$

where $\hat{G}(\mathbf{x}, s; \mathbf{x}_k)$ is the Green's function satisfying

$$\begin{aligned} &\Delta \hat{G} - \frac{(\kappa+s)}{D}\hat{G} = -\delta(\mathbf{x}-\mathbf{x}_k)\,, \quad \mathbf{x}\in\Omega\,,\\ &\hat{G} \sim \frac{1}{4\pi|\mathbf{x}-\mathbf{x}_k|} + \hat{R}_k + o(1)\,, \quad \text{as} \quad \mathbf{x}\to\mathbf{x}_k\,,\\ &\partial_n \hat{G} = 0\,, \quad \mathbf{x}\in\partial\Omega\,, \end{aligned} \tag{6.8}$$

where $\hat{R}_k(s)$ is the regular part of $\hat{G}$, which depends on $\mathbf{x}_k$. It readily follows that the inverse Laplace transform is

$$G_h(\mathbf{x}, t; \mathbf{x}_k) = D^{-1}\mathcal{L}^{-1}\left[\hat{G}(\mathbf{x}, s; \mathbf{x}_k)\right]\,, \tag{6.9}$$

where $G_h(\mathbf{x}, t; \mathbf{x}_k)$ is the heat kernel for Ω defined by the solution to

$$\begin{aligned} &\partial_t G_h = D\Delta G_h - \kappa G_h\,, \quad \mathbf{x}\in\Omega\,,\\ &G_h(\mathbf{x}, 0; \mathbf{x}_k) = \delta(\mathbf{x}-\mathbf{x}_k)\,; \quad \partial_n G_h = 0\,, \quad \mathbf{x}\in\partial\Omega\,. \end{aligned} \tag{6.10}$$

We remark that for the unit sphere, $\hat{G}$ and $\hat{R}_k$ can be determined analytically as (see equations (3.13) and (3.14) of [39])

$$\hat{G}(\mathbf{x}, s; \mathbf{x}_k) = \frac{e^{-\alpha|\mathbf{x}-\mathbf{x}_k|}}{4\pi|\mathbf{x}-\mathbf{x}_k|} + \hat{G}_p(\mathbf{x}, s; \mathbf{x}_k)\,, \tag{6.11a}$$

where $\alpha \equiv \sqrt{(s+\kappa)/D}$ is the principal branch of the square root and where

$$\hat{G}_p = \sum_{n=0}^{\infty} \frac{(2n+1)\beta_n}{4\pi\sqrt{|\mathbf{x}||\mathbf{x}_k|}} P_n(\cos\omega)\, I_{n+1/2}(\alpha|\mathbf{x}|)\, I_{n+1/2}(\alpha|\mathbf{x}_k|)\,. \tag{6.11b}$$

In (6.11b), $\cos(\omega)$ and the coefficients β_n are defined by

$$\cos(\omega) = \frac{\mathbf{x}\cdot\mathbf{x}_k}{|\mathbf{x}||\mathbf{x}_k|}\,, \quad \beta_n \equiv \frac{\alpha K_{n+3/2}(\alpha) - nK_{n+1/2}(\alpha)}{\alpha I_{n+3/2}(\alpha) + nI_{n+1/2}(\alpha)}\,, \tag{6.11c}$$

$P_n(z)$ are Legendre polynomials, and $I_{n+1/2}(z)$ and $K_{n+1/2}(z)$ are modified Bessel functions of the first and second kind. By letting $\mathbf{x} \to \mathbf{x}_k$ in (6.11), we use $P_n(1) = 1$ to identify the regular part in (6.8) as

$$\hat{R}_k(s) = -\frac{\alpha}{4\pi} + \frac{1}{4\pi|\mathbf{x}_k|}\sum_{n=0}^{\infty}(2n+1)\beta_n\left[I_{n+1/2}(\alpha|\mathbf{x}_k|)\right]^2\,. \tag{6.12}$$

Next, by letting $\mathbf{x} \to \mathbf{x}_j$ in (6.7) we enforce that the limiting behavior agrees with that required in (6.6). This yields for each $j = 1, \ldots, m$ that

$$\frac{\hat{b}_j(s)}{D}\hat{R}_j(s) + \sum_{k\neq j}^{m}\frac{\hat{b}_k(s)}{D}\hat{G}(\mathbf{x}_j, s; \mathbf{x}_k) = \hat{B}_j(s)\,. \tag{6.13}$$

Upon using the leading order term $\hat{b}_j = \gamma_j\hat{u}_{j1} + O(\varepsilon)$ from (6.5b), we obtain that

$$\hat{B}_j(s) \sim \frac{\gamma_j}{D}\hat{u}_{j1}(s)\hat{R}_j(s) + \sum_{k\neq j}^{m}\frac{\gamma_k}{D}\hat{u}_{k1}(s)\hat{G}(\mathbf{x}_j, s; \mathbf{x}_k) + O(\varepsilon)\,. \tag{6.14}$$

Finally, we invert the Laplace transform using (6.9) and the convolution property to obtain for $j = 1, \ldots, m$ that

$$\begin{aligned} B_j(t) = \frac{\gamma_j}{D}&\int_0^t u_{j1}(\tau)\, R_j(t-\tau)\, d\tau\\ &+ \sum_{k\neq j}^{m}\gamma_k\int_0^t u_{k1}(\tau)\, G_h(\mathbf{x}_j, t-\tau, \mathbf{x}_k)\, d\tau\,, \end{aligned} \tag{6.15}$$

where $R_j(t) = \mathcal{L}^{-1}\left[\hat{R}_j(s)\right]$. The integro-differential system for the intracellular kinetics $\mathbf{u}_j(t)$, with initial value $\mathbf{u}_j(0) = 0$, is obtained by substituting (6.15) into (6.4).

We emphasize that for the sphere, where analytical formulae for the Laplace transforms of $R_j(t)$ and $G_h(\mathbf{x}_j, t, \mathbf{x}_k)$ are available (see (6.11) and (6.12)), it should be possible to use the *sum-of-exponentials* (cf. [40], [41], [42]) approximation in the Laplace transform plane for the convolution kernels in (6.15) in order to develop a time-marching scheme for the intracellular dynamics. This is the topic of ongoing work.

6.1. The Well-Mixed Limit

In a bounded domain, the coupling between the cells becomes stronger as the bulk diffusivity D increases since the signalling molecule mediating intercellular interactions cannot escape to infinity as in $\mathbb{R}^3$.

In particular, when $D = D_0/\varepsilon \gg 1$ and when the influx permeability parameter is on the range $d_{1j} = O(\varepsilon^{-1})$, we now show that (6.4) and (6.5) reduces to leading-order to the strongly coupled well-mixed limiting system (3.1).

For $D = D_0/\varepsilon$ and $\tilde{d}_{1j} = d_{1j}/\varepsilon$, we have to leading-order from (6.5a) that $B_j = B_c$ for $j = 1, \ldots, m$. By expanding

$$U = U_0 + \frac{1}{D}U_1 + \cdots\,, \tag{6.16}$$

where $U_0 = B_c$ we obtain that U_1 satisfies

$$\begin{aligned} &\Delta U_1 = U_0' + \kappa U_0 - \sum_{j=1}^{m} b_j\delta(\mathbf{x}-\mathbf{x}_j)\,, \quad \mathbf{x}\in\Omega\,,\\ &\partial_n U_1 = 0\,, \quad \mathbf{x}\in\partial\Omega\,, \end{aligned} \tag{6.17}$$

where $b_j = b_j(t)$ from (6.5b) is given in terms of $\tilde{d}_{1j}$ and D_0 by

$$b_j = \gamma_j u_{j1} - \gamma_j \frac{\tilde{d}_{1j}}{d_{2j}} B_j \,, \quad \text{where} \quad \gamma_j = \frac{4\pi d_{2j} D_0}{\tilde{d}_{1j} + D_0} \,. \tag{6.18}$$

From the divergence theorem applied to (6.17) we get that $U_0' = -\kappa U_0 + |\Omega|^{-1} \sum_{j=1}^{m} b_j$. Together with (6.4), this yields the leading-order well-mixed system of (3.1) given by

$$\begin{aligned} U_0' &= -\kappa U_0 - \frac{1}{|\Omega|} \sum_{j=1}^{m} \left(\gamma_j \frac{\tilde{d}_{1j}}{d_{2j}} U_0 - \gamma_j u_{j1} \right) \,, \\ \frac{\mathrm{d}\mathbf{u}_j}{\mathrm{d}t} &= \mathbf{F}_j\left(\mathbf{u}_j\right) - \gamma_j u_{j1} \mathbf{e}_1 + \frac{\tilde{d}_{1j}}{d_{2j}} \gamma_j U_0 \mathbf{e}_1 \,, \end{aligned} \tag{6.19}$$

where $|\Omega|$ denotes the volume of Ω. We emphasize that in this well-mixed limit where $D = D_0/\varepsilon$ and $d_{1j} = \tilde{d}_{1j}/\varepsilon$, the intercellular interactions are $O(1)$ as $\varepsilon \to 0$. This is in contrast to the $D = O(1)$ regime where intercellular interactions are only $O(\varepsilon) \ll 1$.

7. Discussion

We have extended the coupled 2-D cell-bulk ODE-PDE model of [18, 23, 24] to a 3-D bounded domain, where the cells are small spheres of a common radius that are spatially segregated within the domain. Our model is related to the 3-D cell-bulk model formulated in [19, 20, 25] in all of $\mathbb{R}^3$, where there was a single intracellular species within each cell and where the bulk medium was purely diffusive. In a bounded 3-D domain, and in the limit of large bulk diffusivity $D = D_0/\varepsilon$, where $D_0 = O(1)$ and $\varepsilon \ll 1$, the method of matched asymptotic analysis was used to reduce the cell-bulk ODE-PDE model to a novel ODE system for the average bulk chemical concentration that still retains the diffusion parameter D_0 and an $O(\varepsilon)$ correction term that depends on the spatial configuration of the cells through the Neumann Green's matrix. For a spherical domain, where this Green's matrix can be evaluated analytically, and for two-component Sel'kov-type intracellular reaction-kinetics, we showed from our ODE system that both quorum-sensing and diffusion-mediated communication can occur. We emphasize that our new ODE system is distinct from the type of ODE system with global coupling that is usually formulated in the well-mixed limit $D \to \infty$ to study quorum-sensing behavior, where spatial heterogeneity is neglected and there is no diffusivity parameter.

For the leading-order dynamics of our ODE system, where the spatial configuration of cells is neglected, we used the Kuramoto order parameter to study the degree of phase synchronization in the intracellular dynamics as a cell density parameter $\rho = m/|\Omega|$ increases for a fixed population of $m = 1000$ cells. The cell population was composed of two groups: identical cells and *defective* cells, the latter of which have a random parameter in the Sel'kov reaction kinetics. For all the scenarios considered, and as similar to the results in section 4.2 of [24], the cell density parameter was shown to play a dual role of both triggering and quenching intracellular oscillations. Synchronous oscillations are triggered through quorum sensing when the cell density crosses a specific threshold, and are extinguished when the cell density parameter exceeds a further threshold. The QS behavior observed here leads to a roughly switch-like transition of the cells from a quiescent state to perfect phase synchronization. The range of ρ where nearly perfect phase synchronization occurs was shown to decrease as the heterogeneity in the cell population increases. This observation conforms with the usual belief that it is more difficult to trigger intracellular oscillations for a population of non-identical cells (cf. [26], [27]).

Furthermore, for a small population of six cells, we studied the effect of the spatial configuration of the cells on their intracellular dynamics by including the $O(\varepsilon)$ correction terms of the novel ODE system (2.18) in our analysis. These correction terms incorporate the spatial locations of the cells into the ODE system. Their coefficients can be rather significant even for moderately small values of ε and, as a result, we showed that they played an important role in studying quorum-sensing and diffusion-mediated intercellular communication.

There are several possible extensions of the modeling framework and analysis provided in this paper. Firstly, for our novel ODE system, which incorporates weak spatial heterogeneity, it would be interesting to consider the influence of a single defective cell with different reaction-kinetics or membrane permeabilities on a population of identical cells, similar to that studied for the 2-D problem in [23, 24]. In particular, can a single defective cell either extinguish or trigger intracellular oscillations in the entire group of cells? Secondly, the development of a viable numerical approach to numerically solve the 3-D cell-bulk model, in order to confirm the asymptotic results, should be undertaken. This validation was done for the 2-D case in [23] using the commercial solver *FLEXPDE*, but the 3-D problem is more challenging owing to the need for a 3-D refined mesh near the localized cells combined with accurate long-time integrations of oscillatory solutions. Thirdly, it is an interesting open problem to identify chimera type states in our near-well-mixed limiting ODE system (2.18). For a collection of identical cells, where the only heterogeneity arises from the cell locations at $O(\varepsilon)$, we expect that chimera states should be possible when there are two or more distinct groups of closely spaced cells and when κ is rather large. When κ is large, the communication between the groups of cells should be weak, allowing for asynchronous oscillations between the groups. The possibility of such chimera-type states should be examined systematically.

Next, for the regime of finite diffusion where $D = O(1)$ it would be worthwhile to extend the time-marching approach developed in [29] for the integro-differential ODE system for the cell-bulk model in $\mathbb{R}^2$ to our 3-D setting. In particular, by using the *sum-of-exponentials* approximation together with Duhamel's integral, it should be possible to develop an accurate time-marching scheme to numerically solve the integro-differential system (6.15) and (6.4). Without such an approach, it is computationally very inefficient to numerically solve (6.15) and (6.4) with a standard time-discretization since $O(m^2)$ convolution integrals with full memory dependence would have to be evaluated at time t to advance the solution one time-step to time $t + \Delta t$. Moreover, the convolution integrals in (6.15) are improper integrals that need a careful analysis, where the local behavior near the integrable singularity is approximated analytically. The approach used in [29] for the analogous 2-D cell-bulk model in $\mathbb{R}^2$ overcame both of these challenges.

Finally, from the viewpoint of more realistic quorum-sensing modeling in biology, it would be worthwile to apply our analysis to some specific intracellular signalling pathways relevant to applications such as glycolytic oscillations in yeast cells [9, 43] or the *Lux* kinetics used to model bioluminescence behavior [8] and [17]. Moreover, in many quorum-sensing applications it is known that the onset of collective intracellular dynamics is a precursor to the migration or drift of localized cells, which occurs on a longer time-scale, to form some cell colony. Although our asymptotic analysis requires that cells are well-separated, in principle we can impose a dynamical behavior for the center of each cell in terms of the local dipole moment near each cell in order to study the initial stage of cell amalgamation. This dipole moment can be derived from a higher-order asymptotic analysis near each cell. In [8] a phenomenological rule was imposed to model the dynamics of the cell centers in an agent-based model of quorum-sensing.

Acknowledgments

Michael J. Ward gratefully acknowledges the support of the NSERC Discovery Grant Program of Canada. We are grateful to the referees for their helpful comments that improved the initial manuscript.

Appendices

A. Non-dimensionalization of the cell-bulk model

In this appendix we non-dimensionalize the cell-bulk (1.1) into its dimensionless form in (1.2). The dimensions, labeled by $[\ldots]$, of the quantities in (1.1) are

$$[\mathcal{U}] = \frac{\text{moles}}{\text{length}^3}\,, \quad [D_B] = \frac{\text{length}^2}{\text{time}}\,, \quad [\mu_j] = [\mu_c] = \text{moles}$$
$$[k_R] = [k_B] = \frac{1}{\text{time}}\,, \quad [\mathbf{X}] = \text{length} \quad [T] = \text{time}\,,$$
$$[\beta_{1j}] = \frac{\text{length}}{\text{time}}\,, \quad [\beta_{2j}] = \frac{1}{\text{time} \times \text{length}^2}\,.$$

We assume that the common radius R of the cells Ω_j for $j = 1, \ldots, m$ is small compared to the length-scale L of Ω, and so we introduce a small parameter $\varepsilon \equiv R/L \ll 1$. In addition, we introduce the t, $\mathbf{x}$, U and $\mathbf{u}$ by

$$U = \frac{L^3}{\mu_c}\mathcal{U}\,, \quad \mathbf{x} = \frac{\mathbf{X}}{L}\,, \quad t = k_R T\,, \quad \mathbf{u}_j = \frac{\mu_j}{\mu_c}\,, \tag{A.1}$$

so that the time-scale is chosen based on the reaction kinetics. We find that the dimensionless bulk diffusion field satisfies (1.2a), while on the cell boundary (1.1c) becomes

$$D\,\partial_{n_x} U = \frac{\beta_{1j}}{Lk_R}\,U - \frac{\beta_{2j}L^2}{k_R}\,u_{j1}\,, \quad \mathbf{x} \in \partial\Omega_{\varepsilon_j}\,. \tag{A.2}$$

Similarly, by using $\mathrm{d}S_{\mathbf{X}} = L^2 \mathrm{d}S_{\mathbf{x}}$, the dimensional intracellular kinetics (1.1d) transforms to

$$\frac{d\mathbf{u}_j}{dt} = \mathbf{F}_j(\mathbf{u}_j) + \mathbf{e}_1 \int_{\partial\Omega_{\varepsilon_j}} \left(\frac{\beta_{1j}}{Lk_R} - \frac{L^2\beta_{2j}}{k_R}\,u_{j1} \right) \mathrm{d}S_{\mathbf{x}}\,, \tag{A.3}$$

where $\partial\Omega_{\varepsilon_j}$ is the surface of a sphere of radius ε. Since $|\partial\Omega_{\varepsilon_j}| = O(\varepsilon^2)$, in order to ensure that there is an $O(1)$ efflux out of the j^{th} cell into the bulk medium, we must consider the limit where $\beta_{2j}L^2/k_R = O(\varepsilon^{-2})$. Moreover, the feedback into the j^{th} cell from the bulk is $O(\varepsilon)$ when the dimensionless influx parameter is on the asymptotic range $\beta_{1j}/(Lk_R) = O(\varepsilon^{-1})$. Based on these observations, we chose the permeability scalings as in (1.3). With this choice, (A.2) and (A.3) become (1.2c) and (1.2d), respectively.

B. Cell locations

Here, we give the coordinates of the centers of the cells for the different configurations considered in this paper.

B.1. Arbitrarily located cells on a sphere of radius r_0

In Table 1 below, we give the coordinates of $m = 6$ cells on the surface of the unit sphere (corresponding to $r_0 = 1$). These coordinates can be used to generate the centers of cells on any sphere of radius $0 < r_0 < 1$ by scaling appropriately.

Cell i	x_i	y_i	z_i	color code
1	−0.1639	−0.8138	0.5576	black
2	0.9691	−0.1934	−0.1531	green
3	−0.5636	−0.1124	0.8184	red
4	−0.4022	0.7875	−0.4671	blue
5	0.5681	0.4443	−0.6927	cyan
6	−0.6892	−0.5772	−0.4380	magenta

Table 1: Coordinates of the center of $m = 6$ cells arbitrarily located on the surface of the unit sphere. Colors corresponds to color codes for the cells in Fig. 14.

In Table 2 we give the center-to-center distances between the cells with coordinates in Table 1.

B.2. Arbitrarily located cells inside the unit sphere

In Table 3 and Table 4 we give the coordinates of the centers of $m = 6$ identical cells arbitrarily located inside the unit sphere, their distance from the origin, and their center-to-center distances.

References

[1] S. De Monte, F. d'Ovidio, S. Danø, P. Sørensen, Dynamical quorum sensing: Population density encoded in cellular dynamics, PNAS 104 (2007) 18377–18381.

[2] S. Danø, P. Sørensen, F. Hynne, Sustained oscillations in living cells, Nature 402 (1999) 320–322.

[3] S. Danø, P. Sørensen, et al., Quantitative characterization of cell synchronization in yeast, PNAS 104 (2007) 12732–12736.

[4] T. Gregor, K. Fujimoto, N. Masaki, S. Sawai, The onset of collective behavior in social amoebae, Science 328 (2010) 1021–1025.

[5] V. Nanjundiah, Cyclic amp oscillations in dictyostelium discoideum: models and observations, Biophys. Chem. 72 (1998) 1–8.

[6] A. Goldbeter, Biochemical oscillations and cellular rhythms: the molecular bases of periodic and chaotic behaviour, Cambridge university press, 1997.

[7] M. E. Taga, B. L. Bassler, Chemical communication among bacteria, PNAS 100 (2003) 14549–14554.

[8] P. Melke, P. Sahlin, A. Levchenko, H. Jönsson, A cell-based model for quorum sensing in heterogeneous bacterial colonies, PLoS Comput. Biol. 6 (2010) e1000819.

[9] P. Mina, M. di Bernardo, N. J. Savery, K. Tsaneva-Atanasova, Modelling emergence of oscillations in communicating bacteria: a structured approach from one to many cells, J. Royal Soc. Interface 10 (2013) 20120612.

[10] K. Kamino, K. Fujimoto, S. Sawai, Collective oscillations in developing cells: Insights from simple systems, Development, growth & differentiation 53 (2011) 503–517.

[11] M. R. Tinsley, A. F. Taylor, Z. Huang, F. Wang, K. Showalter, Dynamical quorum sensing and synchronization in collections of excitable and oscillatory catalytic particles, Physica D 239 (2010) 785–790.

[12] M. R. Tinsley, A. F. Taylor, Z. Huang, K. Showalter, Emergence of collective behavior in groups of excitable catalyst-loaded particles: spatiotemporal dynamical quorum sensing, Phys. Rev. Lett. 102 (2009) 158301.

[13] A. F. Taylor, M. R. Tinsley, K. Showalter, Insights into collective cell behaviour from populations of coupled chemical oscillators, Phys. Chem. Chem. Phys. 17 (2015) 20047–20055.

[14] A. F. Taylor, M. R. Tinsley, F. Wang, Z. Huang, K. Showalter, Dynamical quorum sensing and synchronization in large populations of chemical oscillators, Science 323 (2009) 614–617.

[15] J. D. Dockery, J. P. Keener, A mathematical model for quorum sensing in pseudomonas aeruginosa, Bull. Math. Biol. 63 (2001) 95–116.

[16] J. P. Ward, J. R. King, A. J. Koerber, P. Williams, J. M. Croft, R. E. Sockett, Mathematical modelling of quorum sensing in bacteria, Math Medicine and Biol. 18 (2001) 263–292.

[17] W. Ridgway, M. J. Ward, B. T. Wetton, Quorum-sensing induced transitions between bistable steady-states for a cell-bulk ODE-PDE model with Lux intracellular kinetics, J. Math. Bio. 84 (2021).

[18] J. Gou, M. Ward, An asymptotic analysis of a 2-D model of dynamically active compartments coupled by bulk diffusion, J. Nonlin. Sci. 26 (2016) 979–1029.

[19] J. Müller, C. Kuttler, B. A. Hense, M. Rothballer, A. Hartmann, Cell–cell communication by quorum sensing and dimension-reduction, J. Math. Bio. 53 (2006) 672–702.

[20] J. Müller, H. Uecker, Approximating the dynamics of communicating cells in a diffusive medium by ODEs—homogenization with localization, J. Math. Bio. 67 (2013) 1023–1065.

[21] B. W. Li, C. Fu, H. Zhang, X. Wang, Synchronization and quorum sensing in an ensemble of indirectly coupled chaotic oscillators, Phys. Rev. E. 86 (2012) 046207.

[22] B. W. Li, X. Z. Cao, C. Fu, Quorum sensing in populations of spatially extended chaotic oscillators coupled indirectly via a heterogeneous environment, J. Nonlin. Sci. 27 (2017) 1667–1686.

[23] S. Iyaniwura, M. Ward, Synchrony and oscillatory dynamics for a 2-D PDE-ODE model of diffusion-sensing with small signaling compartments, SIAM J. Appl. Dyn. Sys. 20 (2021) 438–499.

[24] S. Iyaniwura, M. J. Ward, Localized signaling compartments in 2-D coupled by a bulk diffusion field: Quorum sensing and synchronous oscillations in the well-mixed limit, Europ. J. Appl. Math. 32 (2021) 1001–1031.

[25] H. Uecker, J. Müller, B. A. Hense, Individual-based model for quorum sensing with background flow, Bull. Math. Bio. 76 (2014) 1727–1746.

[26] S. H. Strogatz, From Kuramoto to Crawford: exploring the onset of synchronization in populations of coupled oscillators, Physica D 143 (2000) 1–20.

[27] A. Arenas, A. Diaz-Guilera, J. Kurths, Y. Moreno, C. Zhou, Synchronization in complex networks, Physics Reports 469 (2008) 93–153.

[28] Y. Zhang, J. L. Ocampo-Espindola, I. Z. Kiss, A. Motter, Random heterogeneity outperforms design in network synchroniza-

Cell color	Black	Green	Red	Blue	Cyan	Magenta
Black	0	1.474	0.848	1.916	1.919	1.150
Green	1.474	0	1.818	1.715	0.927	1.726
Red	0.848	1.817	0	1.578	1.968	1.346
Blue	1.916	1.715	1.578	0	1.054	1.395
Cyan	1.919	0.927	1.968	1.054	0	1.634
Magenta	1.150	1.726	1.346	1.395	1.634	0

Table 2: The center-to-center distance between the cells presented in Table 1 for $r_0 = 0.85$. *Colors corresponds to color codes for the cells in Fig. 14.*

Cell i	x_i	y_i	z_i	Distance from origin	Color code
1	−0.2336	0.1684	−0.6002	0.6657	black
2	−0.4370	0.5739	0.2368	0.7592	green
3	0.5784	−0.0731	0.5103	0.7748	red
4	−0.3054	−0.1425	0.0993	0.3513	blue
5	0.4521	−0.2760	−0.6256	0.8197	cyan
6	−0.4092	0.4664	−0.1933	0.6499	magenta

Table 3: Coordinates of the center of $m = 6$ *cells arbitrarily located inside the unit sphere, and their distances from the origin.*

Cell color	Black	Green	Red	Blue	Cyan	Magenta
Black	0	0.9520	1.3967	0.7688	0.8175	0.5340
Green	0.9520	0	1.2347	0.7413	1.5022	0.4442
Red	1.3967	1.2347	0	0.9772	1.1608	1.3272
Blue	0.7688	0.7413	0.9772	0	1.0569	0.6835
Cyan	0.8175	1.5022	1.1608	1.0569	0	1.2165
Magenta	0.5340	0.4442	1.3272	0.6835	1.2165	0

Table 4: The center-to-center distance between the six cells given in Table 3.

tion, PNAS 118 (2021) e2024299118.

[29] M. Pelz, M. J. Ward, Synchronized memory-dependent intracellular oscillations for a cell-bulk ode-pde model in $\mathbb{R}^2$, to appear, SIAM J. Appl. Dyn. Sys. (2024) 50 pages.

[30] M. J. Ward, Spots, traps, and patches: Asymptotic analysis of localized solutions to some linear and nonlinear diffusive systems, Nonlinearity 31 (2018) R189.

[31] J. H. Merkin, D. J. Needham, S. K. Scott, Oscillatory chemical reactions in closed vessels, Proc. Roy. Soc. London. Series A, Mathematical and Physical Sciences 406 (1986) 299–323.

[32] E. E. Sel'kov, Self-oscillations in glycolysis 1. A simple kinetic model, Europ. J. Biochem. 4 (1968) 79–86.

[33] A. Dhooge, W. Govaerts, Y. A. Kuznetsov, MATCONT: a MATLAB package for numerical bifurcation analysis of ODEs, ACM Trans. Math. Soft. (TOMS) 29 (2003) 141–164.

[34] S. H. Strogatz, Nonlinear dynamics and chaos: With applications to Physics, Biology, Chemistry, and Engineering, Westview Press, 2001.

[35] L. F. Shampine, M. W. Reichelt, The MATLAB ODE suite, SIAM J. Sci. Comput. 18 (1997) 1–22.

[36] S. Shinomoto, Y. Kuramoto, Phase transitions in active rotator systems, Progress of Theor. Phys. 75 (1986) 1105–1110.

[37] A. Weber, Y. Prokazov, W. Zuschratter, M. Hauser, Desynchronisation of glycolytic oscillations in yeast cell populations, PLoS ONE 7 (2012) e43276.

[38] A. Cheviakov, M. J. Ward, Optimizing the principal eigenvalue of the Laplacian in a sphere with interior traps, Math. and Comput. Model. 53 (2011) 1394–1409.

[39] R. Straube, M. J. Ward, Intracellular signalling gradients arising from multiple compartments: A matched asymptotic expansion approach, SIAM J. Appl. Math. 70 (2009) 302–332.

[40] G. Beylkin, L. Monzón, On approximation of functions by exponential sums, Appl. and Comput. Harm. Anal. 19 (2005) 17–48.

[41] G. Beylkin, L. Monzón, Approximation by exponential sums revisited, Appl. and Comput. Harm. Anal. 28 (2010) 131–140.

[42] S. Jiang, L. Greengard, S. Wang, Efficient sum-of-exponentials approximations for the heat kernel and their applications, Adv. Comput. Math. 41 (2015) 529–551.

[43] M. A. Henson, D. Müller, M. Reuss, Cell population modelling of yeast glycolytic oscillations, Biochem. J. 368 (2002) 433–446.